Pergamon

Geochimica et Cosmochimica Acta, Vol. 66, No. 9, pp. 1549–1567, 2002

0016-7037/02 $22.00 + .00

PII S0016-7037(01)00875-4

Quantitative Zn speciation in a contaminated dredged sediment by μ-PIXE, μ-SXRF, EXAFS spectroscopy and principal component analysis

MARIE-PIERRE ISAURE,[1,2] AGNÈS LABOUDIGUE,[1] ALAIN MANCEAU,[2,*] GÉRALDINE SARRET,[2] CHRISTOPHE TIFFREAU,[1] PATRICK TROCELLIER,[3] GÉRALDINE LAMBLE,[4] JEAN-LOUIS HAZEMANN,[2] and DANIEL CHATEIGNER[5]

[1]CNRSSP, 930 boulevard Lahure, BP537, 59505 Douai cedex, France
[2]Environmental Geochemistry Group, LGIT, University J. Fourier and CNRS, BP53, 38041 Grenoble cedex 9, France
[3]Laboratoire Pierre Süe, CEA-CNRS, Centre d'Etudes de Saclay, 91191 Gif-sur-Yvette cedex, France
[4]Advanced Light Source, Lawrence Berkeley National Laboratory, University of California, Berkeley, CA 94720, USA
[5]LPEC, Université du Maine-Le Mans, av. O. Messiaen, BP535, 72085 Le Mans cedex, France

(*Received April* 19, 2001; *accepted in revised form October* 8, 2001)

Abstract—Dredging and disposal of sediments onto agricultural soils is a common practice in industrial and urban areas that can be hazardous to the environment when the sediments contain heavy metals. This chemical hazard can be assessed by evaluating the mobility and speciation of metals after sediment deposition. In this study, the speciation of Zn in the coarse (500 to 2000 μm) and fine (<2 μm) fractions of a contaminated sediment dredged from a ship canal in northern France and deposited on an agricultural soil was determined by physical analytical techniques on raw and chemically treated samples. Zn partitioning between coexisting mineral phases and its chemical associations were first determined by micro-particle-induced X-ray emission and micro-synchrotron-based X-ray radiation fluorescence. Zn-containing mineral species were then identified by X-ray diffraction and powder and polarized extended X-ray absorption fine structure spectroscopy (EXAFS). The number, nature, and proportion of Zn species were obtained by a coupled principal component analysis (PCA) and least squares fitting (LSF) procedure, applied herein for the first time to qualitatively (number and nature of species) and quantitatively (relative proportion of species) speciate a metal in a natural system.

The coarse fraction consists of slag grains originating from nearby Zn smelters. In this fraction, Zn is primarily present as sphalerite (ZnS) and to a lesser extent as willemite (Zn_2SiO_4), Zn-containing ferric (oxyhydr)oxides, and zincite (ZnO). In the fine fraction, ZnS and Zn-containing Fe (oxyhydr)oxides are the major forms, and Zn-containing phyllosilicate is the minor species. Weathering of ZnS, Zn_2SiO_4, and ZnO under oxidizing conditions after the sediment disposal accounts for the uptake of Zn by Fe (oxyhydr)oxides and phyllosilicates. Two geochemical processes can explain the retention of Zn by secondary minerals: uptake on preexisting minerals and precipitation with dissolved Fe and Si. The second process likely occurs because dissolved Zn and Si are supersaturated with respect to Zn phyllosilicate. EXAFS spectroscopy, in combination with PCA and LSF, is shown to be a meaningful approach to quantitatively determining the speciation of trace elements in sediments and soils. *Copyright © 2002 Elsevier Science Ltd*

1. INTRODUCTION

Because of physical and chemical erosion of rocks, sediments, and soils, and urban and industrial wastes, waterways generally silt up and require periodic dredging. Dredged sediments are usually deposited on soils along adjacent banks. When sediments contain heavy metals, this practice is hazardous because toxic elements can migrate to the underlying soil and groundwater. The chemical risk resulting from the presence of heavy metals depends on their mobility and bioavailability and therefore on their electronic structure (e.g., oxidation state) and crystal chemistry. The speciation of metals in solids is evaluated classically by chemical extraction procedures (Tessier et al., 1979; Quevauviller et al., 1994; Singh et al., 1998). However, it is now widely recognized that this indirect and operational approach should be complemented by physical techniques, which allow direct identification of metal forms. Extended X-ray absorption fine structure (EXAFS) spectroscopy is of value for this purpose because of its element specificity, sensitivity to short-range ordering, and low detection limit (a few tens of parts per million for Zn; Manceau et al., 1996, 2000; Hesterberg et al., 1997; O'Day et al., 1998, 2000; Ostergren et al., 1999). However, a major obstacle in using EXAFS is its lack of species selectivity (the obtained signal is a weighted average of all metal forms) and sensitivity to minor forms, which can be the most toxic. In this study, these limitations were circumvented for the first time by combining (a) chemical selective extraction procedures, (b) elemental mapping by micro-particle-induced X-ray emission (μ-PIXE) (Mesjasz-Przybylowicz et al., 1999; Xenophontos et al., 1999) and micro-synchrotron-based X-ray radiation fluorescence (μ-SXRF) (Bertsch et al., 1997; Manceau et al., 2000), and (c) rigorous statistical analysis of EXAFS spectra using principal component analysis (PCA) (Wasserman, 1997; Wasserman et al., 1999; Ressler et al., 2000). In soils, metals are often bound to phyllosilicates containing low-Z elements and to Fe and Mn (oxyhydr)oxides. Consequently, the EXAFS signal from phyllosilicates is generally obscured by the intense scattering of Fe and Mn atoms (Manceau et al., 2000). This difficulty was overcome by enhancing the signal from layered minerals using polarized EXAFS (P-EXAFS) measurements on self-support-

* Author to whom correspondence should be addressed (manceau@obs.ujf-grenoble.fr).

ing films of the clay fraction from the sediment (Manceau et al., 1998, 2000; Schlegel et al., 1999, 2001a, 2001b). The studied sediment was dredged from the Scarpe canal near the city of Douai in northern France. This region was selected because it hosted the third largest nonferrous smelter in the world during the first half of the 20th century, and it has released huge amounts of dusts and residues to the environment.

2. EXPERIMENTAL

2.1. Samples

The contaminated sediment was collected with a drill and immediately deposited on a soil and sampled as described in Tiffreau et al. (1999). Samples were air dried and wet sieved in deionized water at 2 mm, 500 μm, 200 μm, 50 μm, and 20 μm. The clay fraction (<2 μm) was isolated by sedimentation of the <20-μm fraction, and the fine fraction (<0.2 μm) was separated by ultracentrifuging the <2-μm fraction. Macroscopic observation of the coarse fraction (500 to 2000 μm) showed that it is highly heterogeneous (Fig. 1). It consists of nonporous black slags (NPBS) (20 wt.%), porous black slags (PBS) (40 wt.%), colored vitreous grains (CG) (27 wt.%), white grains (WG) (8 wt.%) composed mainly of quartz and shell fragments (carbonates), red grains (RG) (4 wt.%) composed mainly of brick residues, and organic particles (OP) (1 wt.%). The NPBS, PBS, and CG show evidence of gas cavities and fluidal morphologic textures. Consequently, at least 87% of the coarse particles present in the sediment are anthropogenic. Each class of grains was separated under a binocular microscope for determining Zn speciation. All fractions and classes of grains were finely dry ground in an agate mortar for bulk chemical analyses. The 500- to 2000-μm fraction was also wet ground in a mechanical agate grinder to evaluate whether oxidation occurred during this stronger grinding procedure.

2.2. Chemical Analyses

Sediment samples were digested by adding 9 mL of HF and 1 mL of HNO_3 to 0.5 g of solid in a Teflon bomb and heating at 200°C for 1 h in a microwave oven. After evaporation of the solution, 3 mL of 6 N HCl was added to the residue for final dissolution. Element concentrations were measured by inductively coupled plasma atomic emission spectroscopy (ICP-AES).

2.3. Chemical Treatments

Chemical treatments aimed at selectively dissolving Zn species but not phyllosilicates were applied to the <2-μm fraction. Oxidation-sensitive species (i.e., organic matter and sulfides) were extracted with H_2O_2 following the procedure described in Jackson (1985). Fe (oxy-hydr)oxides were removed with a dithionite-citrate solution buffered with sodium bicarbonate (CBD) (pH = 7.3; Mehra and Jackson, 1960). This reducing treatment was applied only one time to prevent dissolution of other mineral phases. The oxidative and reductive treatments were applied either separately or successively to remove all redox-sensitive species. The percentages of elements extracted by these chemical treatments were determined from their concentrations in the solid and extracted solutions as measured by ICP-AES.

2.4. X-ray Diffraction

Mineral identifications was performed using a Siemens D501 powder diffractometer with Co Kα radiation (40 kV and 37.5 mA). X-ray powder diffraction patterns of the nonclayey fraction were recorded over 5 to 90° 2θ with a 0.04° 2θ step and a 20-s counting time per point. Clay fractions were prepared as oriented slides, and X-ray diffraction (XRD) patterns were recorded for both air-dried and ethylene-glycol-saturated states from 2 to 50° 2θ at a 0.04° 2θ interval using a 6-s counting time per point.

2.5. Microprobe Analyses

μ-PIXE and μ-SXRF analyses were performed on coarse particles (500 to 2000 μm) and the clay fraction (<2 μm), respectively. μ-SXRF was preferred over μ-PIXE for the fine fraction analyses because of its better lateral resolution. The μ-PIXE measurements were carried out at the nuclear microprobe facility of the Pierre Süe Laboratory in Saclay, France (Trocellier, 1996) on NPBS, PBS, and CG prepared as 30-μm-thick thin sections embedded in epoxy resin. Elemental maps were recorded using a 3.07-MeV $^4He^+$ beam, and samples were rastered in a 4-μm step through a 4×4 μm sized focused beam with a typical beam current of 200 pA and a cumulated charge of 2.5 μC. Selected Kα fluorescence radiations for Zn, Fe, and S were collected using a Si(Li) solid state detector with a 100-ms counting time per point. Elemental concentrations of selected points on the chemical map were calculated using the Gupix software (Maxwell et al., 1989). The μ-SXRF maps were recorded on the 10.3.2. beamline at the Advanced Light Source in Berkeley, California (McDowell et al., 1998). They were measured on clay fractions prepared as oriented slides scanned with a 2-μm step through a 2×2 μm sized focused X-ray beam. Selected Kα fluorescence radiations for Zn, Fe, and S were collected using a solid state detector and a 4-s counting time per point.

2.6. EXAFS Spectroscopy

Pressed pellets from the dry-ground raw sediment (Raw), the dry-ground (DGC) and wet-ground (WGC) whole coarse fraction, and the dry-ground NPBS, PBS, and CG fractions were prepared for bulk EXAFS measurements. EXAFS spectra of individual grains for nonporous black slags, porous black slags, and colored grains (NPBSg1, NPBSg2, PBSg, and CGg) prepared as thin sections were also recorded. Samples of the two finest fractions, including the raw (Raw $<$ 2μm), the CBD-treated (CBD $<$ 2μm), the H_2O_2- and CBD-treated (H_2O_2 + CBD $<$ 2μm), and the <0.2-μm fractions (<0.2 μm), were prepared as self-supporting films for P-EXAFS. The orientation distributions of basal planes of clay minerals within self-supporting films were determined by quantitative texture analysis (i.e., texture goniometry), as described elsewhere (Manceau et al., 1998, 2000). As an illustration, the radial distribution of the orientation densities of c* axes off the film normal for the H_2O_2 + CBD $<$ 2μm sample is presented in Figure 2. This distribution shows an evolution of the orientation density, reaching a maximum of 7.2 m.r.d. (multiple of a random distribution) perpendicular to the film plane ($\rho = 0$) and a minimum of 0 m.r.d. near $\rho = 80°$. The full width at half maximum of the distribution is 58.9°, which is significantly larger than the values of 23.1 to 39.9° reported by Manceau et al. (2000) on soil clay fractions. However, theoretical calculations showed that the texture strength is still high enough to observe a polarization dependence of P-EXAFS spectra.

Zn K-edge X-ray absorption spectra were measured at room temperature on the BM32 beamline at the European Synchrotron Radiation Facility in Grenoble, France. The X-ray absorption of samples was measured either in transmission detection mode with photodiodes or in fluorescence-yield mode with a 30-element Ge solid-state detector (Canberra), depending on Zn concentration. X-ray absorption spectra of the NPBSg1, NPBSg2, PBSg, and CGg individual grains were collected using a 100×40 μm sized X-ray beam in fluorescence-yield mode (Hazemann et al., 1995). Measurements on powdered samples were performed at the magic angle (Manceau et al., 1990) to get rid of the possible preferential orientation of layered minerals in the pellets. Polarized measurements were carried out by mounting self-supporting films on an (X,Y)-goniometer stage. In-plane and out-of-plane X-ray absorption spectra were measured by orienting the plane of the film parallel ($\alpha = 0°$) and perpendicular (grazing incidence, $\alpha = 80°$) to the electric field vector of the X-ray beam, respectively.

The EXAFS functions ($\chi[k]$) were derived from X-ray absorption spectra by modeling the postedge atomic absorption with a spline function and normalizing the signal amplitude to the jump of the sample X-ray absorption. The kinetic energy (E_k) of the photoelectron was converted to wave vector (k) value by taking the energy origin ($E_k = 0$) at the half-height of the K-edge absorption jump. Radial structure functions (RSFs) were obtained by Fourier transforming $k^3\chi(k)$ functions apodized with a Kaiser function (Manceau and Combes, 1988). The abscissae of RSFs graphs ($R + \Delta R$) correspond to interatomic distances uncorrected for phase shift (Teo, 1986).

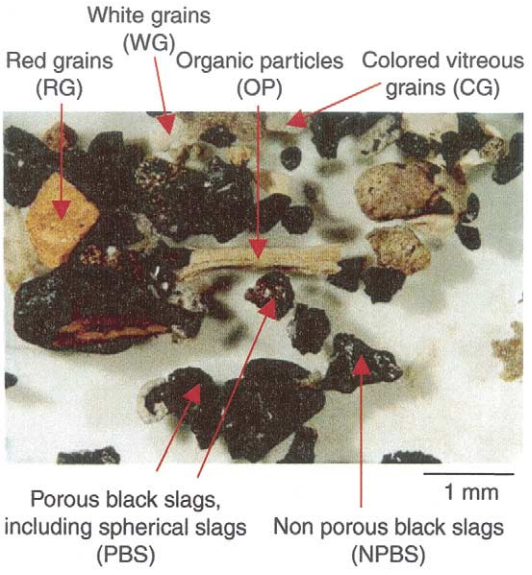

Fig. 1. Coarse fraction (500 to 2000 μm) of the sediment observed with a binocular microscope.

The EXAFS spectra were analyzed in a two-step procedure. The first step consisted of a PCA of the whole set of EXAFS spectra (Fay et al., 1992; Wasserman, 1997; Wasserman et al., 1999; Ressler et al., 2000). Presentation of the fundamentals of this mathematical treatment is clearly beyond the scope of this paper, and interested readers are referred to Malinowski's (1991) textbook. The PCA allows determination of the number of independent components contained in a set of spectra, which corresponds to the number of Zn species (i.e., Zn spectra) statistically meaningful to quantitatively reproduce the series of experimental data. Of course, the total number of metal species has to be lower than the number of spectra, a requirement that was amply satisfied in the present study. The criterion $R = \Sigma\ (k^3\chi_{exp} - k^3\chi_{model}) / \Sigma\ k^3\chi_{exp}$ was used to determine the number of principal components. A component was considered significant when its introduction in the spectral reconstruction process led to decrease of R by at least 20%. The consistency of this procedure was also checked by visual examination of the experimental and reconstructed spectra. Then, an operation called target transformation evaluates whether a reference spectrum is a likely principal component of the system. A large database of Zn-containing mineral species, including pure minerals (carbonates, sulfides, oxides, phosphates, etc.) various Zn-substituted and Zn-sorbed references (phyllosilicates, Fe and Mn (oxyhydr)oxides, etc.; Manceau et al., 2000), and organic compounds (Sarret et al., 1998), was screened to identify Zn species. Ideally, if all unknown species are present in the database, then the number of references selected by this procedure is equal to the number of principal components. In other words, this approach is quite rigorous and tells us (a) if a particular reference is actually present in the unknown sample and (b) how many species are absent in the database and remain unidentified.

The second step consisted of least squares fitting (LSF) of experimental EXAFS spectra to the combination of reference spectra previously identified by PCA. Of course, this second step makes sense only if all unknown species were previously successfully retrieved from the database. The fractional contribution of each model spectrum to the fit is directly proportional to the amount of Zn present in that form in the sample. Uncertainty in the proportion of individual Zn species was estimated from a variation of R amounting to ~15%. This value corresponds to an absolute precision on the proportion of an individual compound of ~10%.

3. RESULTS

3.1. Chemical Analyses

Results from chemical analyses indicate that Zn is preferentially concentrated in the 500- to 2000-μm, 2- to 20-μm, and

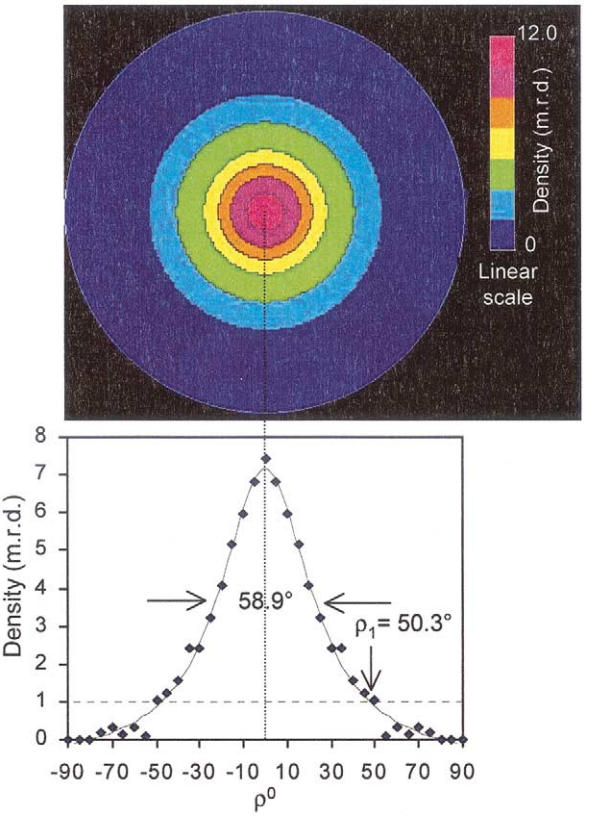

Fig. 2. (001) pole figure and radial orientation distribution densities (ρ scan) of the dispersion of crystallite platelets off the film plane for the H_2O_2 + CBD < 2 μm sample. The strong density maximum at the center of the (001) pole figure (ρ = 0°) indicates that the film has a [001]* fiber texture. Linear density scale and equal area projection are used for the pole figure. The pole density is expressed in multiple of a random distribution (m.r.d.). Points: experimental values; solid line: fit with a Lorentzian function.

<2-μm fractions, which contain ~8400, 11,200, and 16,700 ppm Zn, respectively (Table 1). The amount of zinc in the bulk sample and in the size fractions is well correlated with sulfur (R^2 = 0.88) and not with any other element (for example, R^2 = 0.1 for Zn-Fe). Within the coarse-grain fraction (500 to 2000 μm), Zn concentration varies from ~1800 ppm in OP to ~11000 ppm in the PBS (Table 2). S concentration amounts to 2000 ppm in WG; 7000 to 12,000 ppm in CG, NPBS, and PBS; and up to 110,000 ppm in OP. The highest Fe concentrations are measured in CG (~23,000 ppm) and RG (~49,500 ppm). All grains contain large amounts of Ca, with concentrations up to ~10.7% and 29 wt.% in NPBS and WG, respectively. Therefore, variability in chemical composition corresponds to the variability in shape and color of sediment grains. The 2- to 20-μm fraction is composed of a mixture of clay aggregates and grains similar to coarse grains. Consequently, only the 500- to 2000-μm and the <2-μm fractions were investigated in detail. The <2-μm fraction is enriched in Zn (~16,700 ppm), Fe (~46,500 ppm), S (~21,000 ppm), P (~9500 ppm), Al (61,000 ppm), and Mg (~6000 ppm) compared to the bulk sediment. The mass proportion of Zn in each fraction was calculated from the relative mass of this fraction and its Zn concentration (Figs. 3A and 3B). Results show that the coarse

Table 1. Average concentrations of major and trace elements and mineralogy of the sediment.

Size fraction (μm)	Bulk	500 to 2000	200 to 500	50 to 200	20 to 50	2 to 20	<2	<0.2
wt.%		9	25	14	13	34	5	<0.1
				Elemental concentrations (ppm)				
Na	3100	3500	1800	2000	6700	3000	1700	1600
Mg	3700	6000	1200	1000	3300	4600	6200	9200
Al	28,500	39,300	10,500	10,500	36,100	48,700	61,000	85,900
P	3600	1700	380	1000	2700	6400	9300	1700
S	12,800	7700	2000	4600	7000	17,000	20,600	940
K	9500	13,200	4600	6800	13,700	10,600	12,000	17,100
Ca	50,000	85,900	19,600	20,800	15,000	58,400	34,400	9000
Mn	270	480	120	130	260	390	530	420
Fe	18,400	16,100	4100	4800	17,800	36,300	46,300	61,700
Zn	6600	8400	2400	1300	5500	11,200	16,700	910
Pb	770	1000	300	210	780	1600	1900	2900
				Mineralogy				
	Quartz	Quartz	Quartz	Quartz	Quartz	Quartz	Quartz	Quartz
	Calcite	Calcite	Calcite	Calcite	Microcline	Calcite[a]	Calcite	
	Albite[a]	Albite		Albite[a]		Albite	Albite[a]	
	Microcline[a]	Microline[a]				Microline[a]		
	Hematite[a]	Hematite				Hematite[a]	Sphalerite	
		Willemite					Calcium	
		Sphalerite[a]					Iron oxide[a]	
							Illite	Illite
							Smectite	Smectite
							Kaolinite	Kaolinite
							Chlorite	Chlorite

[a] Trace amounts.

fraction (500 to 2000 μm) contains 11% of total Zn, the 2- to 20-μm fraction 55%, and the <2-μm fraction 12% (Fig. 3C).

3.2. Chemical Extractions

As much as 82% of S and 76% of Zn were removed from the <2-μm fraction by H_2O_2 (Table 3), suggesting a possible Zn-S association, as already inferred from bulk chemical analysis. This treatment also removed a significant part of the Ca (45%) and Mn (14%). The removal of Ca likely results from the dissolution of $CaCO_3$ at the low pH (~2 to 3) of this extraction procedure, as also reported by Shuman (1978). Only 56% of the Fe was removed by the CBD treatment, which is consistent

Table 2. Average concentrations of major and trace elements and mineralogy of grains from the coarse fraction of the sediment.

	NPBS	PBS	CG	RG	WG	OP
wt.%	20	40	27	4	8	1
			Elemental concentrations (ppm)			
Na	3800	4700	4600	5000	750	<dl[a]
Mg	5900	2900	8800	6800	1100	<dl[a]
Al	27,100	31,100	62,200	79,100	5100	<dl[a]
P	200	530	170	1300	610	150,000
S	10,500	12,000	7000	3600	2000	110,000
K	12,700	14,100	20,500	28,300	2000	3900
Ca	107,000	13,500	60,600	29,100	236,000	36,300
Mn	330	360	930	450	340	150
Fe	13,500	14,300	23,100	49,500	2500	6700
Zn	7700	11,000	5000	5100	1900	1800
Pb	820	1400	650	600	120	70
			Mineralogy			
	Quartz	Quartz	Quartz	Quartz	Quartz	na[b]
	Calcite	Calcite	Calcite	Calcite	Calcite	
	Albite[c]	Mullite	Mullite	Hematite	Aragonite[c]	
	Iron phosphate	Albite	Albite[c]	Microcline[c]		

NPBS = nonporous black slags, PBS = porous black slags, CG = colored vitreous grains, RG = red grains, WG = white grains, OP = organic particles.

[a] Under detection limit.

[b] Not analyzed.

[c] Trace amounts.

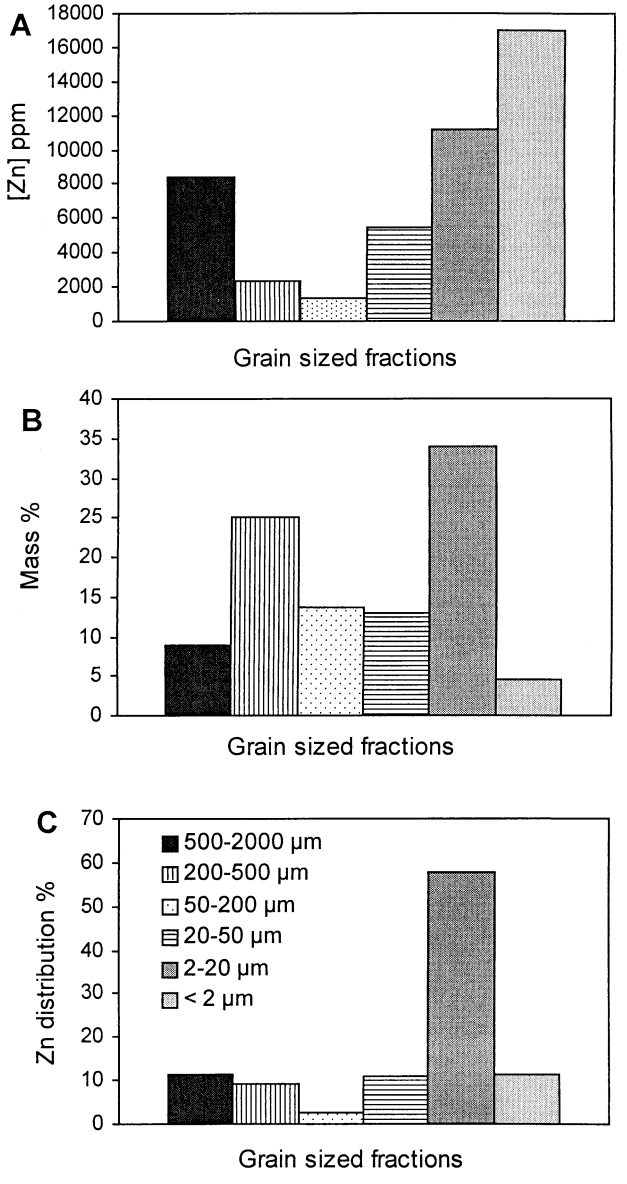

Fig. 3. Concentration of Zn in grain-sized fractions (A), weight percentage of grain-sized fractions (B), and proportion of Zn in grain-sized fractions (C).

with one cycle of treatment. This treatment also extracted 34% of Zn, 65% of P, 48% of Ca, and 27% of Mn. Simultaneous extraction of Zn and Fe suggests that Zn is partly bound to Fe (oxyhydr)oxides, and the parallel extraction of Zn and P could arise from the dissolution of an iron phosphate constituent. The complexation of Ca^{2+} by citrate in solution could explain the high amount of extracted Ca (Stumm and Morgan, 1996). The relatively high amount of Mn extracted by the CBD treatment likely results from the reductive dissolution of manganese oxides, indicating that this treatment is not Fe specific. The sum of Zn separately extracted by H_2O_2 and CBD amounted to ~110%, compared to ~89% when the two extractants were applied successively to the same sample, indicating that the two procedures are almost conservative. In conclusion, despite the less than perfect selectivity of chemical extractants, chemical extractions by H_2O_2, CBD, and H_2O_2 + CBD treatments suggest that Zn is associated predominantly with S and, to a lesser extent, with oxidized Fe or Mn mineral species.

Table 3. Percentages of elements removed by chemical extractions from the <2-μm fraction of the sediment.

	H_2O_2	CBD	H_2O_2 + CBD
Mg	5	5	5
Al	2	4	8
P	0	65	69
S	82	na[a]	na[a]
K	7	15	18
Ca	45	48	73
Mn	14	27	14
Fe	1	56	49
Zn	76	34	89
Pb	2	23	27

CBD = sodium bicarbonate–buffered ditrionite-citrate solution.
[a] Not analyzed.

3.3. XRD

Characteristic XRD patterns from the coarse and clay fractions are presented in Figure 4, and minerals identified by this technique are listed in Tables 1 and 2. Quartz and calcite are predominantly present in the coarse fraction, admixed with minor amounts of albite, microcline, hematite, willemite (Zn_2SiO_4), and sphalerite (ZnS). The XRD pattern shows a broad maximum between 28 and 33° 2θ (3.14 to 4.13 Å) originating from diffusion by amorphous material. In addition to the dominant quartz and calcite, sphalerite, calcium iron oxide, albite, illite, chlorite, kaolinite, and smectite were also detected in the <2-μm fraction. XRD patterns of intermediate size fractions could be described as a mix of the two previous end-member patterns. In summary, two Zn-bearing phases were identified by XRD: willemite and sphalerite.

3.4. μ-PIXE and μ-SXRF

3.4.1. Characterization of Zn-Bearing Coarse Particles

μ-PIXE elemental maps of PBS grains showed that Zn, S, and Fe are irregularly distributed in the grains. The highest Zn concentrations were observed in sulfur-containing localized areas several tens of micrometers across (105,000 ppm Zn, 86,000 ppm S, and 47,000 ppm Fe at point A in Fig. 5), whereas smaller Zn concentrations were observed in Fe-rich zones (14,300 ppm Zn, 300 ppm S, and 48,000 ppm Fe at point B in Fig. 5). In these two point analyses, moderate concentrations of Si (51,000 to 96,000 ppm) and Ca (10,000 to 35,200 ppm) and tiny amounts of the other elements (Mg, K, etc.) were measured. At point C in Figure 5, moderate concentrations of Zn and Fe were measured (44,000 and 21,000 ppm, respectively) with low S, Si, and Ca amounts (5600, 1800, and 9000 ppm, respectively), indicating that Zn is not associated with only Fe and S.

The presence of at least two predominant Zn species in PBS grains was shown in the plot of S vs. Zn intensities by two groups of points, one in which Zn and S are strongly correlated

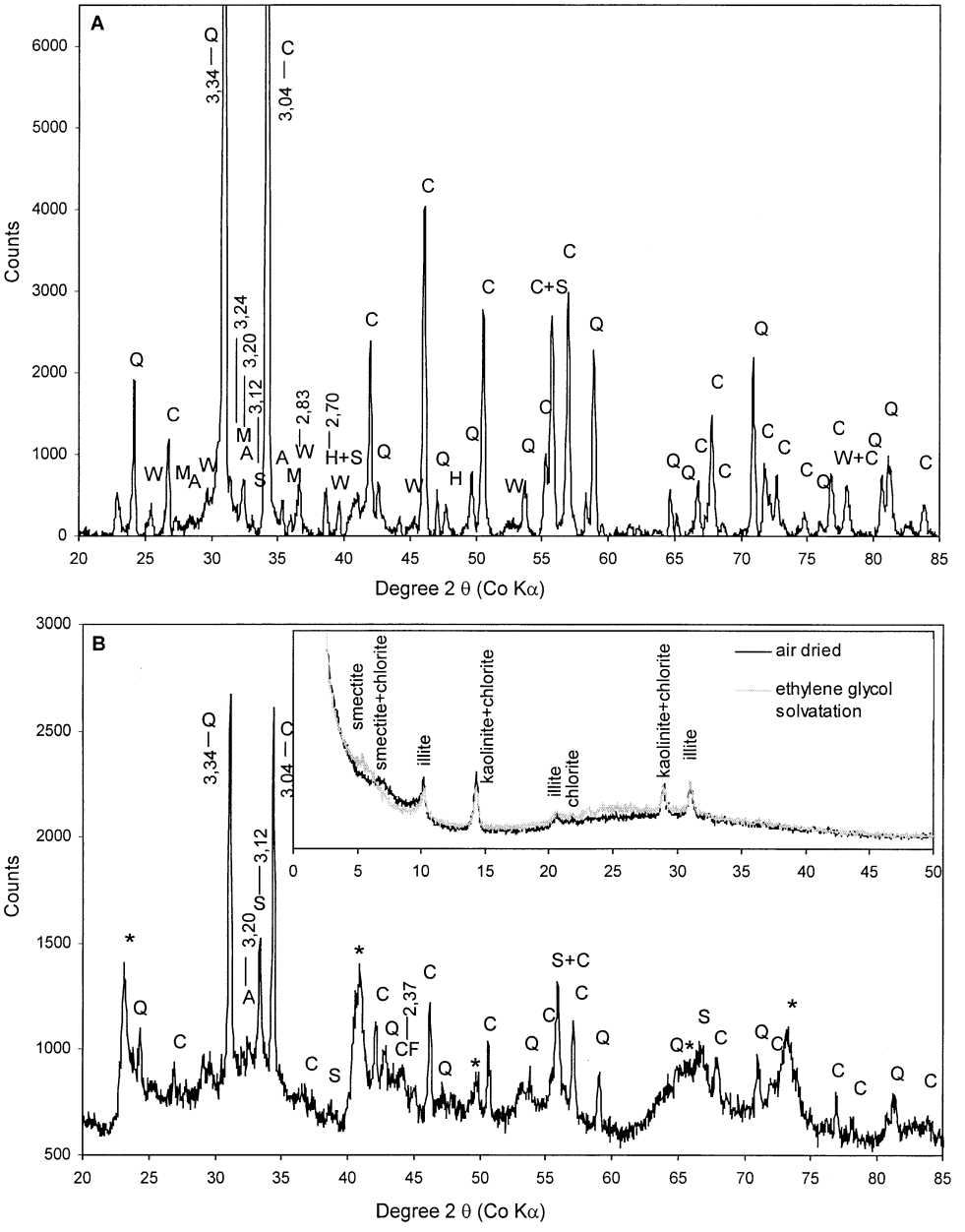

Fig. 4. Powder X-ray diffraction patterns for the coarse (A) and clay (B) fractions of the sediment. Detected phases in (A) are quartz (Q), calcite (C), albite (A), microcline (M), hematite (H), sphalerite (S), and willemite (W). Detected phases in (B) are: quartz, calcite, albite, calcium iron oxide (CF), sphalerite, and phyllosilicates (*). The *d* spacings (Å) of the most intense peaks for each mineral are reported.

(R^2 = 0.80) and a second in which they are not (Fig. 6). No strong correlation was observed between S and Fe and between Zn and Fe (plots not shown). These findings extend to CG, whereas only the Zn-S association was detected in NPBS (data not shown).

3.4.2. *Characterization of Zn-Bearing Fine Particles*

μ-SXRF elemental maps of the <2-μm fraction showed that Zn, S, and Fe are heterogeneously distributed (Fig. 7). High Zn concentrations were found in (S, Fe)-rich grains several micrometers in diameter (points A and B in Fig. 7), but Zn and Fe were also associated in larger and more diffuse areas of the clay matrix. The existence of two Zn chemical associations was confirmed by the plots of μ-SXRF intensities (Fig. 8). The first type of association corresponds to the group of points labeled I and II in Figure 8. In these two groups, Fe and S are strongly correlated (Fig. 8C, R^2 = 0.76 to 0.93) and Zn and Fe (R^2 = 0.63 to 0.66) and Zn and S (R^2 = 0.51 to 0.56) are less correlated (Figs. 8A and 8B). Group I in Figure 8 corresponds to point A in Figure 7 and group II to point B in Figure 7.

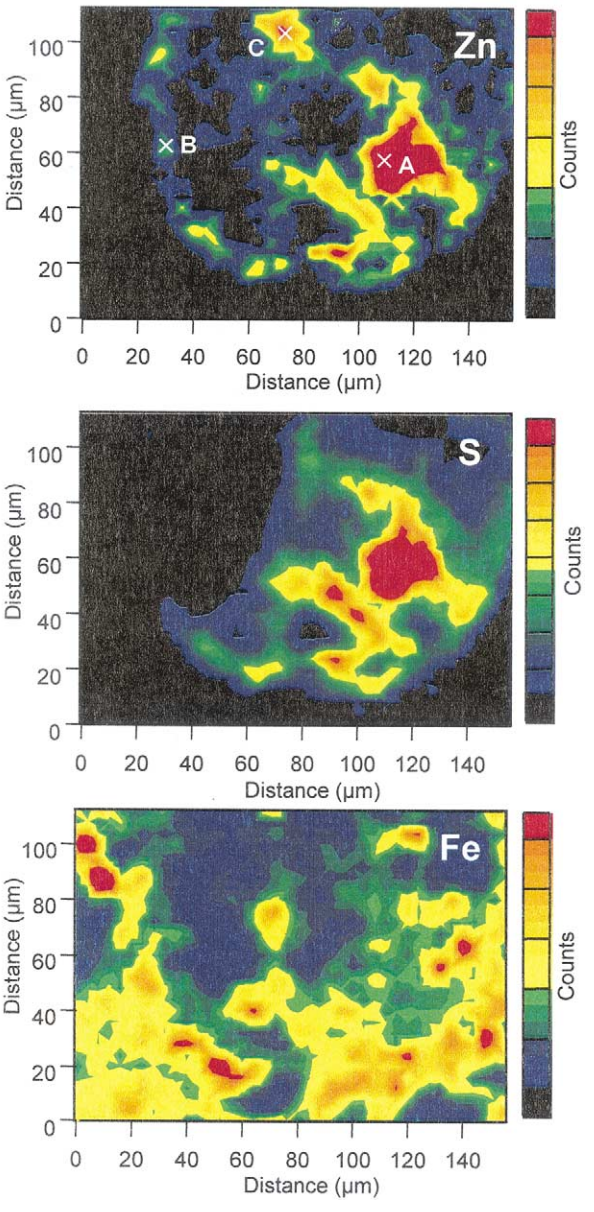

Fig. 5. Zn, S, and Fe micro-particle-induced X-ray emission maps of a porous black slag. Scanning step: 4 μm; count time: 100 ms/point. Concentrations measured in point A are [Zn] ~ 105,000 ppm, [S] ~ 86,000 ppm, and [Fe] ~ 47,000 ppm. Concentrations measured in point B are [Zn] ~ 14,300 ppm, [S] ~ 300 ppm, and [Fe] ~ 48,000 ppm. Concentrations measured in point C are [Zn] ~ 43,900 ppm, [S] ~ 5600 ppm, and [Fe] ~ 21,400 ppm.

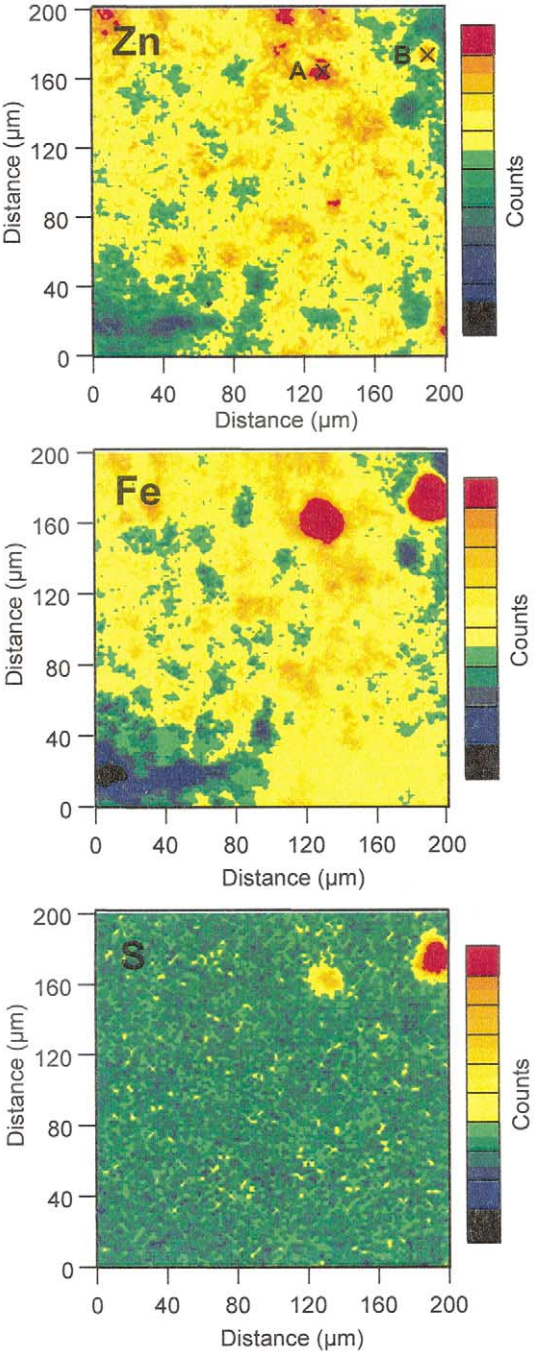

Fig. 7. Zn, S, and Fe micro-synchrotron-based X-ray radiation fluorescence maps of the <2-μm fraction of the sediment. Scanning step: 2 μm; count time: 4 s/point. Points A and B correspond to (Fe, S)-rich grains.

Because they lack other major elements, these grains could correspond to a Zn-Fe-S solid solution or to an intimate mixture of pyrite (FeS_2) and sphalerite, and the two observed correlations (I and II) to a different pyrite/sphalerite ratio. Figure 7 shows that Zn is concentrated preferentially in the center of the grains and Fe in the outer region. This chemical differentiation may result from the initial precipitation of an (Fe, Zn) sulfide solid solution during the smelting process followed by the precipitation of FeS_2 after all the Zn was depleted from the melt. As these sulfide grains are clearly not authigenic but inherited from the smelting process, another explanation is the preferential leaching of Zn from the (Fe, Zn) sulfide grains after their formation. According to this alternative, these grains would have dissolved incongruently because Fe in FeS_2 and Zn in ZnS have the same solubility (logKs, ZnS = −10.9, Dyrssen and Kremling, 1990; logKs, FeS_2 = −16.4, Davison, 1991). The preferential leaching of Zn may have happened in nature or during the sample preparation. These sulfur grains are clearly

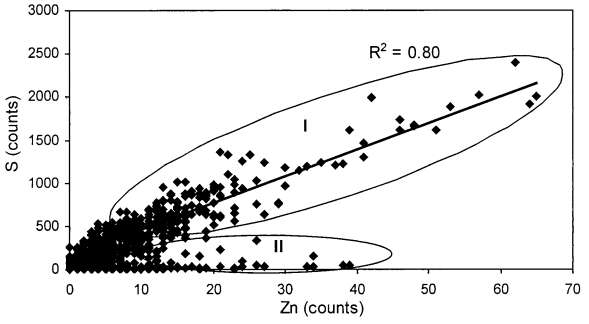

Fig. 6. Plot of S vs. Zn micro-particle-induced X-ray emission intensities for nonporous black slags. Points in group I correspond to (Zn, S)-rich regions such as point A in Figure 5 ($R_2 = 0.80$). Points in group II correspond to the rest of the matrix ($R_2 < 0.005$).

bigger than 2 μm, and consequently, their presence in the clay fraction stems from an imperfect grain-size separation of the $<$2-μm fraction. However, similar grains, but of a smaller size ($<$2 μm), were observed by scanning electron microscopy (SEM) (data not shown), supporting their pervasive presence. The second type of Zn association corresponds to the points that lack S and are reasonably well correlated to Fe (Fig. 8A, $R_2 = 0.56$). In summary, μ-SRXF suggests the existence of two Zn species in the $<$2-μm fraction of the sediment, one containing S and Fe and present as individualized grains, and a second containing Fe, but no S, distributed throughout the clay matrix.

3.5. Powder EXAFS Spectroscopy

Figures 9 and 10 show Zn K-edge EXAFS spectra and RSFs for the raw sediment (Raw), the various size fractions (WGC, DGC, NPBS, PBS, CG, Raw $<$ 2 μm, CBD $<$ 2 μm, H_2O_2 + CBD $<$ 2 μm, and $<$0.2 μm), and some individual grains (NPBSg1, NPBSg2, PBSg, CGg), together with two reference compounds, sphalerite and zincite (ZnO). The CGg spectrum is clearly much different from all others, and its phase, amplitude, and shape were satisfactorily simulated by ZnO weighted by 0.62 (Fig. 9A). Therefore, this grain contains ZnO as the major Zn species. The 38% decrease in amplitude compared to the reference is likely due to a self-absorption effect (Troger et al., 1992; Castaner and Prieto, 1997), since the grains are clearly heterogeneous and locally can contain high Zn concentrations. The decrease in amplitude cannot be attributed to structural disorder because the experimental and ZnO EXAFS spectra have the same shape and, specifically, the same high frequency features. As will be shown below, spectra of the other samples are not affected by this phenomenon. In particular, it was not observed for the ZnS species, and this result is consistent with μRBS measurements, which showed that ZnS is localized in the surface of grains (Isaure et al., 2001).

Significant differences are observed among other EXAFS spectra. For instance, the PBS spectrum has a notable higher frequency and amplitude than the $<$0.2-μm spectrum. Spectra could be classified in three groups on the basis of the position of first RSF peak (Figs. 9B, 10A, and 10B). Samples of the first group include Raw, PBS, PBSg, NPBS, NPBSg1, NPBSg2, Raw $<$ 2 μm, and CBD $<$ 2 μm, and have their first peak

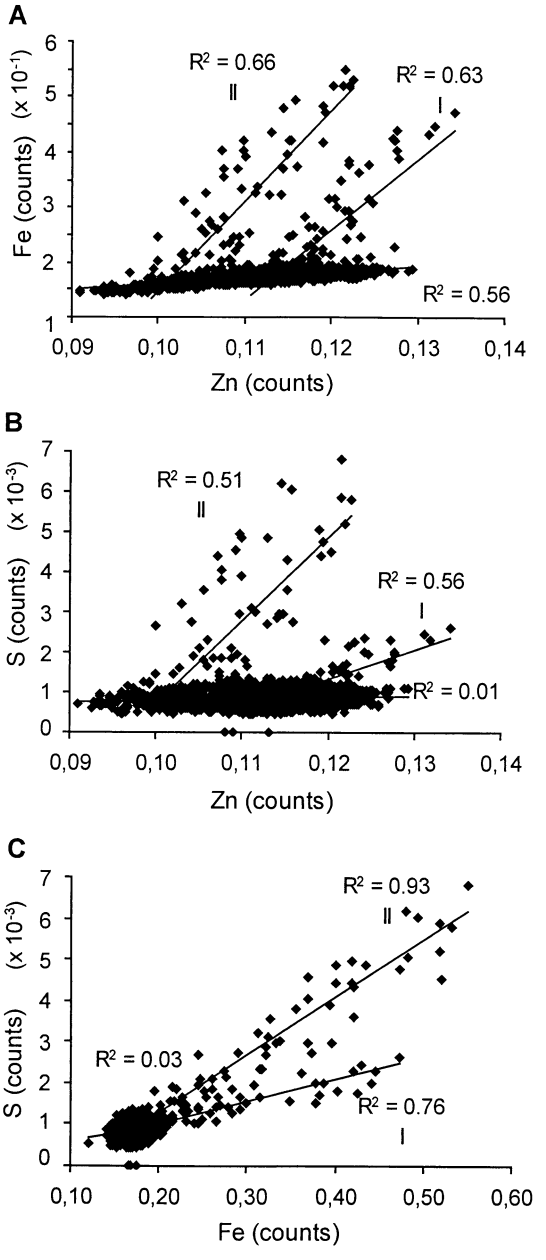

Fig. 8. Plots of Zn, Fe, and S normalized micro-synchrotron-based X-ray radiation fluorescence intensities for the $<$2-μm fraction. Points of groups I and II correspond to (Fe, S)-rich regions such as points A and B in Figure 7 ($R^2 = 0.76$ and 0.93).

centered at $R + \Delta R = 1.96$ Å, as ZnS (Fig. 9B). Samples of the second group encompass CGg, WGC, H_2O_2 + CBD $<$ 2 μm, and $<$0.2 μm, and have their first peak at $R + \Delta R = 1.59$ Å, as ZnO (Fig. 10A). DGC and CG make up the third group and are characterized by a split of the first peak with maxima at $R + \Delta R = 1.59$ Å and $R + \Delta R = 1.96$ Å (Fig. 10B). Considering that the ΔR value is about -0.3 to -0.4 Å (Teo, 1986), an $R + \Delta R$ value of 1.96 Å is typical of the Zn-S bond length (2.34 Å in ZnS). Likewise, the $R + \Delta R = 1.59$ Å value matches the Zn-O bond length (1.96 Å in ZnO).

For the fine fractions (Raw $<$ 2μm, CBD $<$ 2 μm, H_2O_2 +

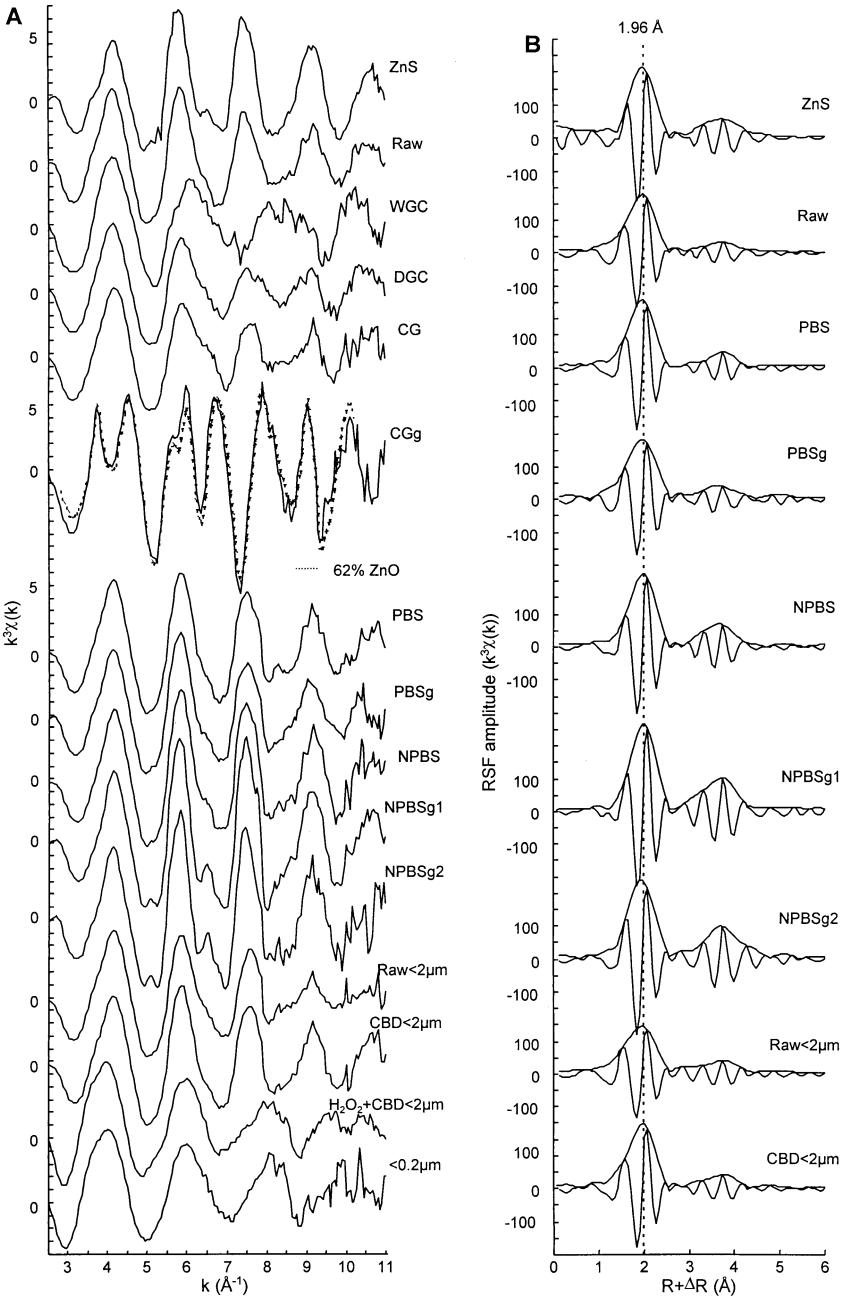

Fig. 9. (A) Zn K-edge extended X-ray absorption fine structure spectroscopy spectra of the series of samples. (B) Radial structure functions (RSFs) for samples having their first RSF peaks at $R + \Delta R = 1.96$ Å.

CBD < 2 μm, and <0.2 μm), no angular dependence of EXAFS spectra was observed. Since texture goniometry indicated that clay particles are significantly oriented in the film plane, this result could be interpreted by the absence of Zn-containing phyllosilicates. However, clear evidence will be given below that Zn is partly bound to phyllosilicates, and the absence of polarization effect suggests that the Zn-clay particles are not aligned in the film plane for a specific reason.

3.5.1. Identification of Zn Species

For a given number of principal components, the higher the number of experimental spectra, the more accurate is the metal species determination. For this reason, PCA analysis was performed on the whole set of spectra except CGg, because preliminary analysis indicated that the ZnO species was only present in CGg.

Figures 11 and 12 show experimental spectra reconstructed

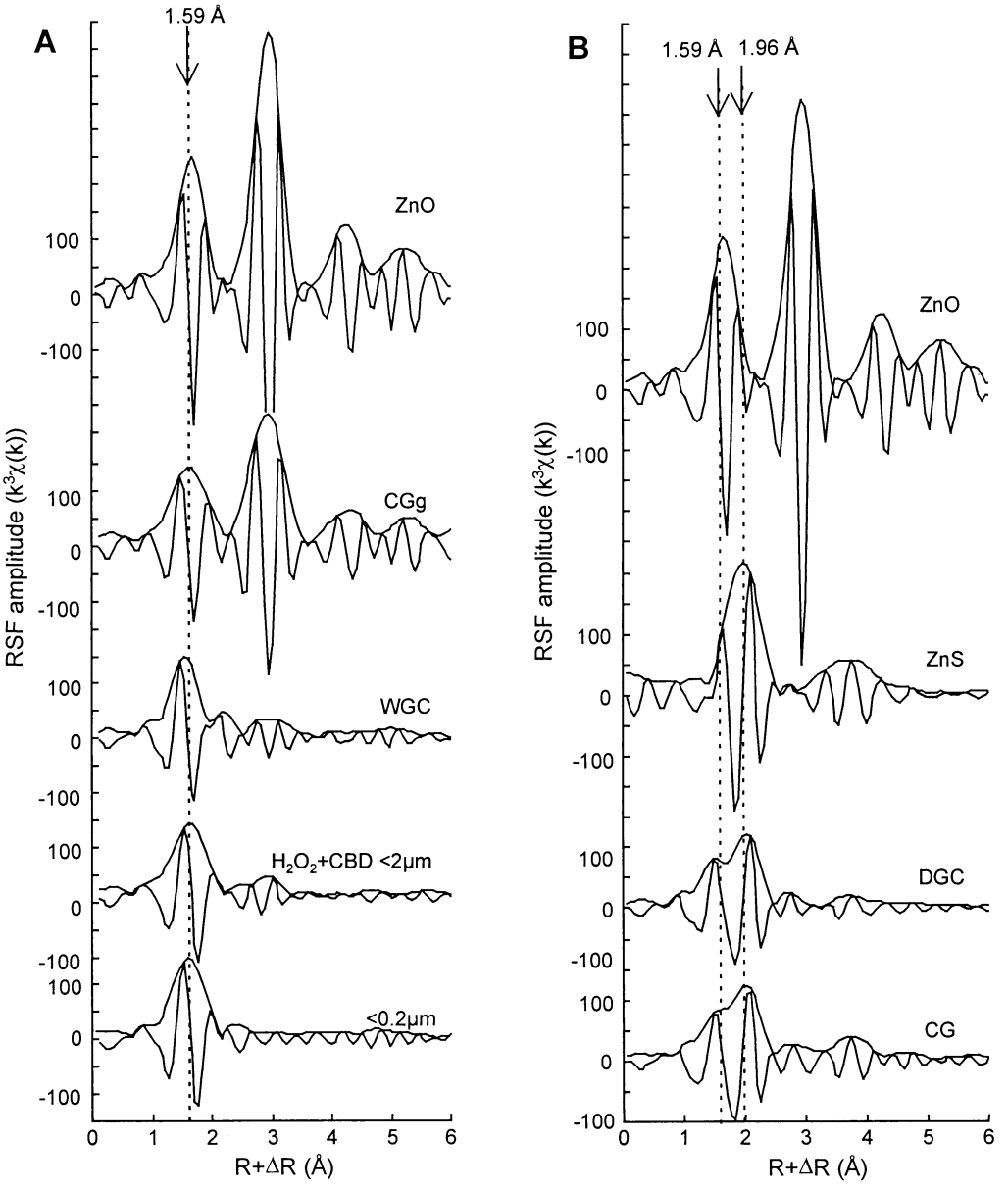

Fig. 10. Radial structure functions (RSFs) for samples having their first RSF peaks at (A) $R + \Delta R = 1.59$ Å and at (B) $R + \Delta R = 1.96$ Å with a shoulder 1.59 Å.

using a combination of the first two, three, and four principal components. The first two components satisfactorily reproduced the majority of sample spectra, except WGC ($R = 0.42$), DGC ($R = 0.22$), CG ($R = 0.28$), H_2O_2 + CBD < 2 μm ($R = 0.39$), and <0.2 μm ($R = 0.28$) in the 2.5- to 10.0-Å^{-1} range (Fig. 11). The WGC ($R = 0.10$) and H_2O_2 + CBD ($R = 0.09$) spectra were well reproduced with the three first components, but this model still failed to account for DGC ($R = 0.13$), CG ($R = 0.18$) and <0.2 μm ($R = 0.13$) in the 7.0- to 8.7-Å^{-1} interval, the 6.3- to 7.8-Å^{-1} interval, and the 5.8- to 7.5-Å^{-1} interval, respectively (Fig. 12A). Finally, adding the fourth and last component improved the simulation of DGC ($R = 0.12$), CG ($R = 0.17$), and <0.2 μm ($R = 0.07$) spectra (Fig. 12B). As is evident from a visual inspection of Figure 12B, this four-component model yielded a better match of the phase in the 7.0- to 8.7-Å^{-1} interval for DGC, the 6.3- to 7.8-Å^{-1} interval for CG, and the 5.8- to 7.5-Å^{-1} interval for <0.2 μm. This improvement of the spectral match did not result in a substantial reduction of the fit residual R factor because the difference between the experimental and the simulated spectra is comparable to the noise level. Consequently, three, and probably four, independent EXAFS spectra (i.e., Zn species) are necessary and sufficient to describe quantitatively the 13 experimental EXAFS spectra. Additional support for the existence of a fourth component will be provided by the LSF procedure.

The four most likely Zn species were then identified by

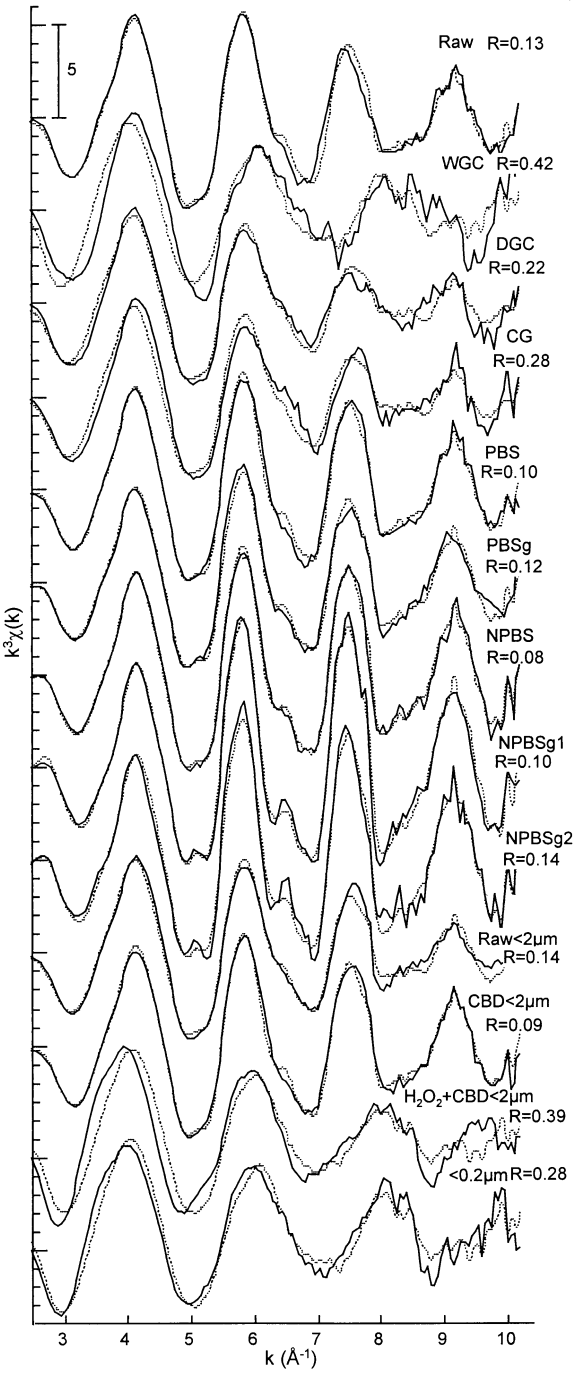

Fig. 11. Experimental Zn K-edge extended X-ray absorption fine structure spectroscopy spectra (solid lines) and two-component reconstructed spectra (dotted lines) for the whole series of samples.

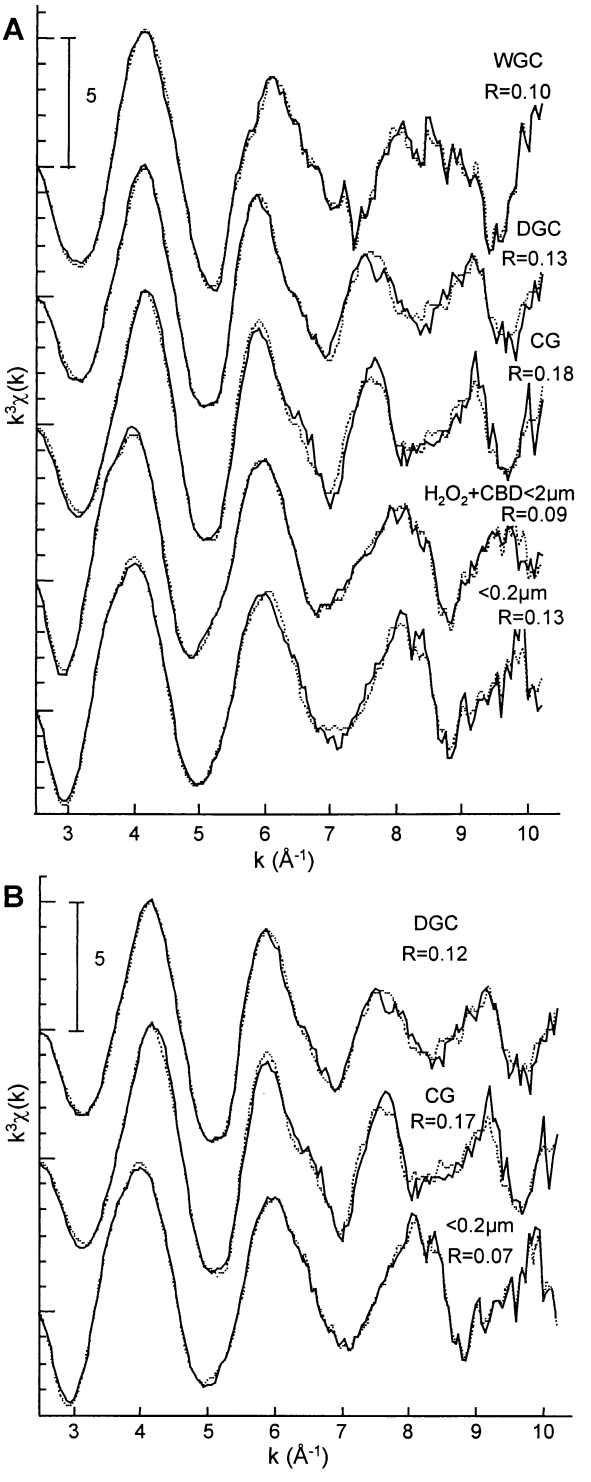

Fig. 12. Experimental Zn K-edge extended X-ray absorption fine structure spectroscopy spectra (solid lines) and three-component (A) or four-component (B) reconstructed spectra (dotted lines) for a selection of samples.

target transformation of reference spectra in our Zn database. The best spectral match was obtained with willemite, sphalerite, Zn-sorbed ferrihydrite (ideally $5Fe_2O_3 0.9H_2O$) (ZnFh) used as a proxy for Zn bound to Fe (oxyhydr)oxides, and the trioctahedral smectite Zn-kerolite ($Si_4[Zn_{0.75}Mg_{2.25}]O_{10}[OH]_2.nH_2O$) (ZnKer) used as a proxy for Zn-containing phyllosilicates (Fig. 13). The spectral agreement is good for willemite (R = 0.19), ZnS (R = 0.20), and ZnFh (R = 0.27), with all features correctly reproduced, and fair for ZnKer (R = 0.33). The reliability of the Zn species determination is assessed in Figure 13 by comparing the ex-

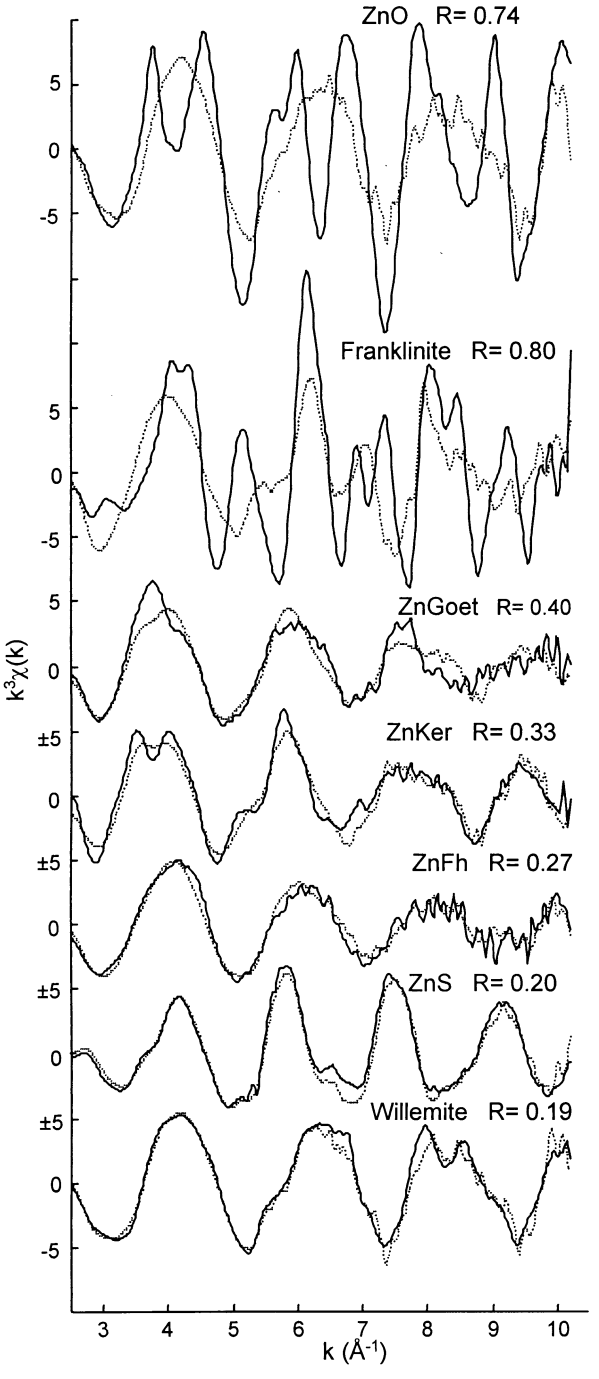

Fig. 13. Target transformation of Zn K-edge extended X-ray absorption fine structure spectroscopy spectra for several Zn references: willemite (Zn_2SiO_4), sphalerite (ZnS), Zn-sorbed ferrihydrite ($5Fe_2O_3 0.9H_2O$, ZnFh), Zn-substituted kerolite ($Si_4[Zn_{0.75}Mg_{2.25}]O_{10}[OH]_2.nH_2O$, ZnKer), Zn-containing goethite (α[Fe, Zn]OOH, ZnGoet), franklinite ($ZnFe_2O_4$), and zincite (ZnO). Solid line: experimental spectra; dotted line: target transformed spectra.

perimental and recalculated spectra for zincite (R = 0.74), franklinite (ZnFe*2O4*, R = 0.80), and Zn-containing goethite (α[Fe, Zn]OOH, R = 0.40). The presence of willemite and sphalerite in the samples is in agreement with XRD results. The Fe (oxyhydr)oxide and phyllosilicate Zn species were not detected by XRD but are positively identified by EXAFS because of its metal specificity and sensitivity to short-range ordering. Note that these two additional species are consistent with the μ-SXRF maps of the <2-μm fraction, which showed that Zn is tightly associated with Fe throughout the clay matrix at the micron scale (natural phyllosilicates generally contain Fe).

3.5.2. Quantification of Zn Species

The proportion of each Zn species in the various samples was then determined by LSF of the experimental EXAFS spectra with linear combinations of the reference spectra. Simulations were performed using, successively, one, two, three, and four Zn species out of the four references previously identified by target transformation. A given fit was retained if the factor of merit R decreased significantly (more than 20%) in comparison to the previous simulation. Visual examination was also used to check the consistency of the fit. Best-fit calculations along with the experimental spectra are shown in Figures 14 and 15 and in Table 4. For example, the one-component fit for the raw sediment was clearly unsatisfactory (Fig. 14A, R = 0.40), and its EXAFS spectrum could be correctly simulated (R = 0.18) by assuming a combination of ZnS and ZnFh. Adding a third component did not improve the fit (R = 0.18, not shown). The frequency between 6.2 and 7.0 $Å^{-1}$ is not reproduced correctly by the simulation because the ZnS reference presents a narrow feature at this energy. The absence of this feature in the sediment spectrum likely originates from a lower crystallinity of ZnS, leading to a loss of higher distance atomic shell correlations and, accordingly, to a decrease of higher frequency wave contributions. Apart from CGg, in which Zn is speciated as ZnO, three Zn species were identified in the coarse fraction: ZnS, ZnFh, and willemite (Fig. 14, Table 4). The distribution of Zn species in the WGC fraction (22% ZnS + 42% ZnFh + 40% willemite) differed from the one found in the DGC fraction (52% ZnS + 30% ZnFh + 20% willemite), indicating that wet grinding partly dissolved ZnS, thus enhancing the sensitivity of EXAFS to residual phases, namely, Fe (oxyhydr)oxides and willemite. The powder (NPBS) and individual grains (NPBSg1 and NPBSg2) of NPBS contain only ZnS (Figs. 14D, 14E, and 14F), whereas both ZnS and ZnFh are present in PBS (PBS and PBSg, Figs. 14G and 14H). This result is in agreement with μ-PIXE, which showed only a Zn-S association in NPBSs (data not shown) and Zn-S and Zn-Fe associations in PBSs (Fig. 5). The powder and individual grains of each black slag fraction have similar proportions of Zn species, which indicates that Zn speciation is homogenous from one grain to another. In contrast, the CG powder could be described by a combination of 51% ZnS + 36% ZnFh + 19% willemite (Fig. 14I), whereas only ZnO was detected in the studied individual grain (CGg). Therefore, the CG chosen for EXAFS analysis was not representative of the CG fraction, and ZnO is thought to amount to less than 10% of total Zn in this fraction. This finding points out the difficulty in sampling heterogeneous systems and the necessity of combining bulk and individual grains or laterally resolved analyses to evaluate the representativity of a particular species. In the present case, the proportion of ZnO in the whole sediment is likely less than a few percent. Given that the majority of Zn in

the coarse fraction is contained in NPBS, PBS, and CG (87%, Table 2), the Zn speciation in NPBS + PBS + CG, weighted by the Zn concentration in each class of grains, should be conservative with that in the coarse fraction (DGC). The relative amount of Zn species calculated for NPBS + PBS + CG is 69% ZnS + 20% ZnFh + 3% willemite (Table 4), compared to 52% ZnS + 30% ZnFh + 20% willemite for DGC. This calculation overestimates ZnS (+17%) and underestimates ferrihydrite (−10%) and willemite (−17%). This discrepancy can be attributed to the omission of the other types of grains (RG, WG, and OP), which represent 13% of total Zn, and to an underestimation of the proportion of CG, which are the richest in willemite. Indeed, gray grains have been classified as NPBS, but they may have a CG-like composition. In conclusion, in the coarse fraction, Zn is partitioned between three major phases, ZnS, Fe (oxyhydr)oxides, and willemite, the proportion of which amounts to ~52, 30, and 20%, respectively.

Two components were sufficient to fit EXAFS spectra of the clay (<2 μm) and fine (<0.2 μm) fractions (Fig. 15). The Raw < 2 μm fraction was correctly fitted with 58% ZnS and 52% ZnFh. These two species were also identified in CBD < 2 μm, but the amount of ZnFh was lower, as expected, because of the partial dissolution of Fe (oxyhydr)oxides during the CBD treatment (Fig. 15B). In these two samples, the narrow feature between 6.2 and 7.0 $Å^{-1}$ was again not correctly reproduced by the simulation, probably because of a lower crystallinity of ZnS in the sediment, as mentioned previously for sample Raw. In H_2O_2 + CBD < 2 μm, there was no ZnS left, and consequently, the minor ZnKer component was revealed together with ZnFh (Fig. 15C). Note that the amount of Zn-ferrihydrite identified in H_2O_2 + CBD < 2 μm accounts for only 11% of the Zn-ferrihydrite detected in Raw < 2 μm because the main part of Zn-ferrihydrite was extracted by the treatment. The untreated <0.2-μm sample contained only ZnKer and ZnFh, indicating that the size of ZnS grains in the sediment is larger than 0.2 μm. ZnFh represents the major pool of Zn in the <0.2-μm fraction (71%, Fig. 15D). Since the fine fraction does contain Zn-bearing phyllosilicates, this species was added to the simulation of Raw < 2 μm, but this three-species model (ZnS + ZnFh + ZnKer) failed to improve the two-species model (ZnS + ZnFh). Therefore, the Zn-phyllosilicate species firmly identified in the chemically treated and size-fractionated sediment samples likely represents less than ~10 to 20% of total Zn in the clay fraction, and even less in the raw sediment. This explains why this species went undetected in the analysis of the Raw sample (Fig. 14A).

4. DISCUSSION

4.1. Speciation of Zn in the Coarse Fraction

In the coarse fraction, sphalerite, willemite, zincite, and Zn-containing Fe (oxyhydr)oxide were identified by EXAFS spectroscopy. Sphalerite, the presence of which was suggested by μ-PIXE, detected by XRD, and quantified by EXAFS spectroscopy, is the major Zn species of this fraction and is localized in smelting residues (black slags and colored vitreous grains). Thiry and Van Oort (1999) showed that in the pyrometallurgical process, up to 20% of zinc can be lost because of incomplete oxidation of ZnS, generating ZnS-containing slags. This mineral was also positively identified by XRD and SEM in dusts emitted by a smelter processing zinc and lead sulfide ores located nearby our sampling site (Sobanska et al., 1999). Although our results unambiguously demonstrate that ZnS arises primarily from anthropogenic activities, ZnS precipitation in the anoxic sediment cannot be dismissed because the measured potential of the dredged sediment was ~180 mV. The occurrence of diagenetic ZnS was also reported by Webb et al. (2000) in Zn-contaminated sediment from Lake DePue, Illinois. ZnS particles were also identified recently by chemical extractions, XRD, and SEM in a stream sediment near a gold mining site in South Korea (Song et al., 1999) and by EXAFS spectroscopy in an anoxic sediments near a mining area in Anglesey, Wales (Parkman et al., 1996) and in estuary sediments contaminated by military and industrial activities in San Francisco Bay, California (O'Day et al., 2000).

Willemite was identified by XRD in the coarse fraction and by EXAFS spectroscopy in the coarse fraction and CG. No Si-Zn correlation was observed by μ-PIXE in CG because of the overwhelming presence of Si in quartz and other silicates (Table 2). Willemite is a high-temperature anhydrous silicate that originates from the smelting processes. This Zn species was detected in smelter-affected soils by XRD (Thiry and Van Oort, 1999) and by XRD and EXAFS (Manceau et al., 2000). The third high-temperature mineral identified in this study is zincite. It is clearly not of paramount importance because it was detected in only one specimen of CG, not in the powdered coarse-grain fraction. This chemical heterogeneity is consistent with the large range of colors exhibited by sediment grains spanning from light blue, green, and gray to darker colors. ZnO is the product of ZnS oxidation in smelters, and it was identified by Sobanska et al. (1999) in smelter dusts and by Thiry and Van Oort (1999) in soils located near a Zn foundry. Therefore, ZnO identified in this study most likely originates from the nearby (Zn, Pb) smelters. Additional evidence for the anthropogenic origin of zincite, willemite and sphalerite is the occurrence of mullite in PBS and CG grains, as indicated by XRD. Indeed, mullite is also a high-temperature mineral that was identified in smelter-affected soils (Thiry and Oort, 1999) and in industrial alumino-silicate ashes (Hammade, 2000).

Zn-sorbed ferrihydrite-like species were pervasive in all coarse particles except NPBS using μ-PIXE and EXAFS spectroscopy. Although EXAFS allows neither firm identification of the nature of the Fe (oxyhydr)oxide Zn is bound to nor determination of its uptake mechanism (e.g., adsorption, lattice substitution), the presence of well-crystallized Zn-substituted Fe (oxyhydr)oxides can be dismissed because they have a distinctly different EXAFS spectrum (Fig. 13; Manceau et al., 2000). Since ferrihydrite is the most common ferric phase formed during the oxidative dissolution of pyrite (FeS_2; Cornell and Schwertmann, 1996; Bigham et al., 1996), and given its high metal sorption capacity (Davis and Kent, 1990; Spadini et al., 1994; Cornell and Schwertmann, 1996; Martinez and McBride, 1998), it is the most probable Zn-containing ferric phase. The weak porosity of NPBS accounts for the absence of secondary phases, such as Zn-sorbed ferrihydrite, in these grains. This Zn species was reported in the bed sediment from an acid mine drainage system (Hochella et al., 1999), in mine tailings containing sphalerite and pyrite, and in contaminated sediments (Song et al., 1999).

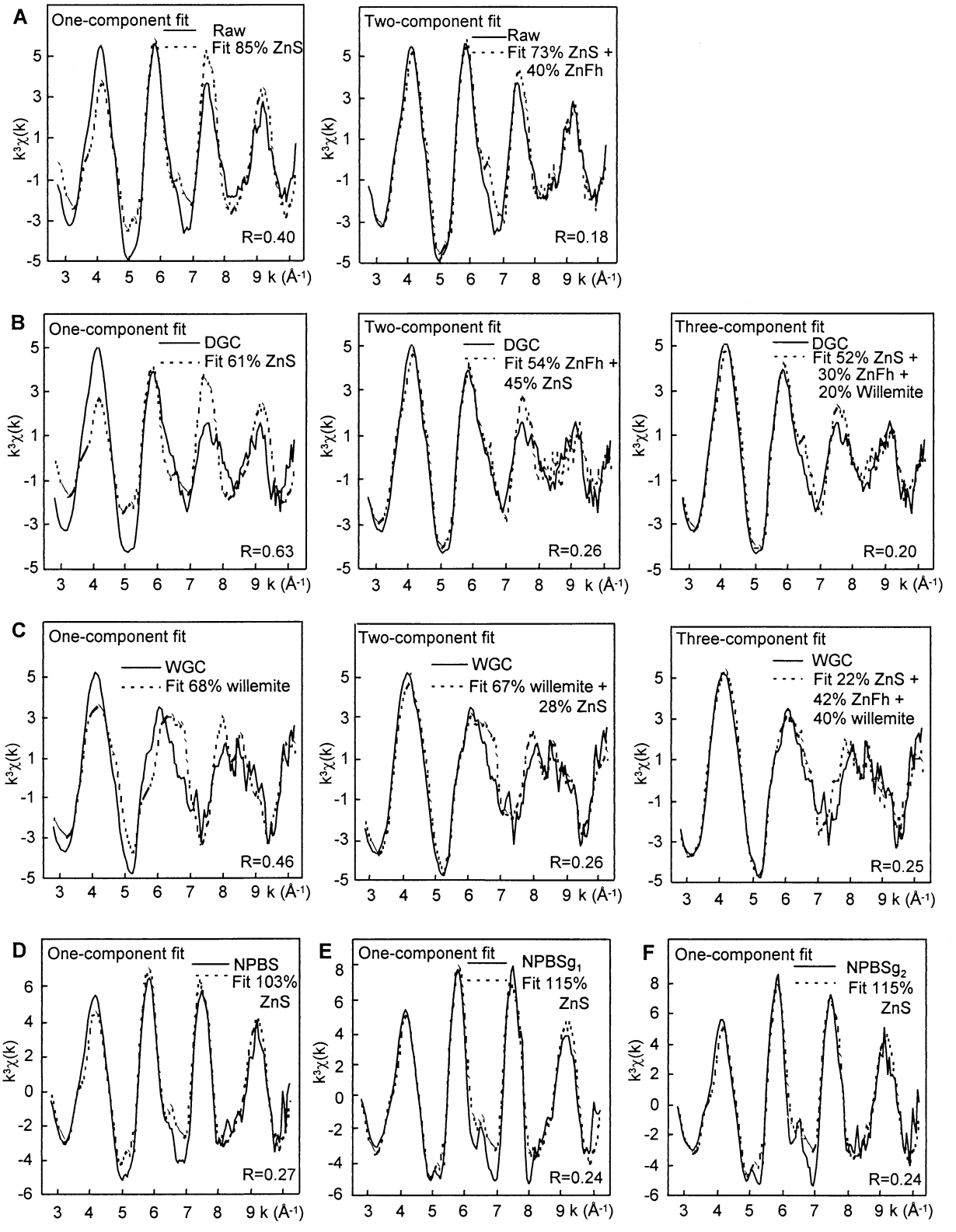

Fig. 14. Least squares fit of extended X-ray absorption fine structure spectroscopy spectra for samples from the coarse fraction with one, or a combination of two or three, Zn references (ZnS, ZnFh, and willemite).

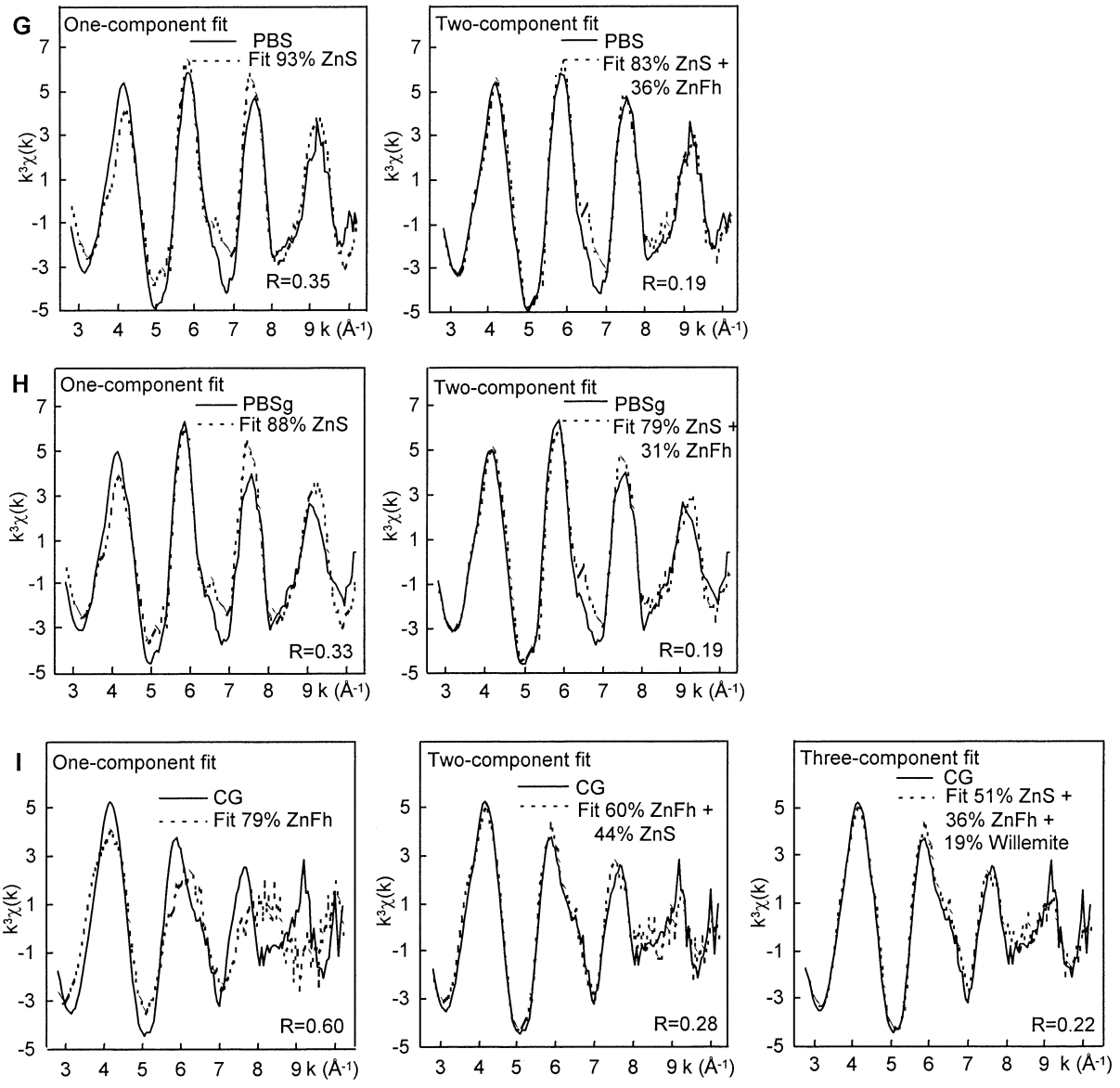

Fig. 14. (Continued)

4.2. Speciation of Zn in the Clay Fraction

In the fine fraction of the sediment, three Zn species were identified: sphalerite, Zn-sorbed ferrihydrite, and Zn-containing phyllosilicate. Size fractionation coupled with μ-SXRF and EXAFS showed that ZnS occurs in grains larger than 0.2 μm. This finding is consistent with the identification by EXAFS spectroscopy, electron microscopy, and secondary ion mass spectrometry of sphalerite grains smaller than 1 μm in sediments from a mine drainage area in the Tri-State Mining District (Kansas, Missouri, and Oklahoma; O'Day et al., 1998). As in the coarse fraction, Zn-sorbed ferrihydrite is thought to result from the weathering of iron and zinc sulfides. The Zn-containing phyllosilicate was readily detected in the $<$0.2-μm fraction, but only after dissolving ZnS and ZnFh in the $<$2-μm fraction. In this dredged sediment, Zn released by the weathering of primary minerals (ZnS, willemite) is essentially taken up by poorly crystallized secondary Fe (oxyhydr)oxides and, to a lesser degree, by phyllosilicates, which amounts to $<\sim$10 to 20% in the fine fraction. The lack of angular dependence observed for raw and chemically treated fine fractions, including H_2O_2 + CBD $<$ 2 μm, in which about half the Zn is bound to phyllosilicates, suggests that the Zn-containing phyllosilicates occur either as coatings on other grains or as extremely fine, gel-like, neoformed clay particles. This finding suggests that this Zn pool coprecipitated with dissolved silica to form poorly crystallized clay particles and did not sorb on preexisting phyllosilicate particles.

4.3. Origin and Fate of Zn

The anthropogenic Zn grains found in this sediment can have several origins. Fine metalliferous particles may have been

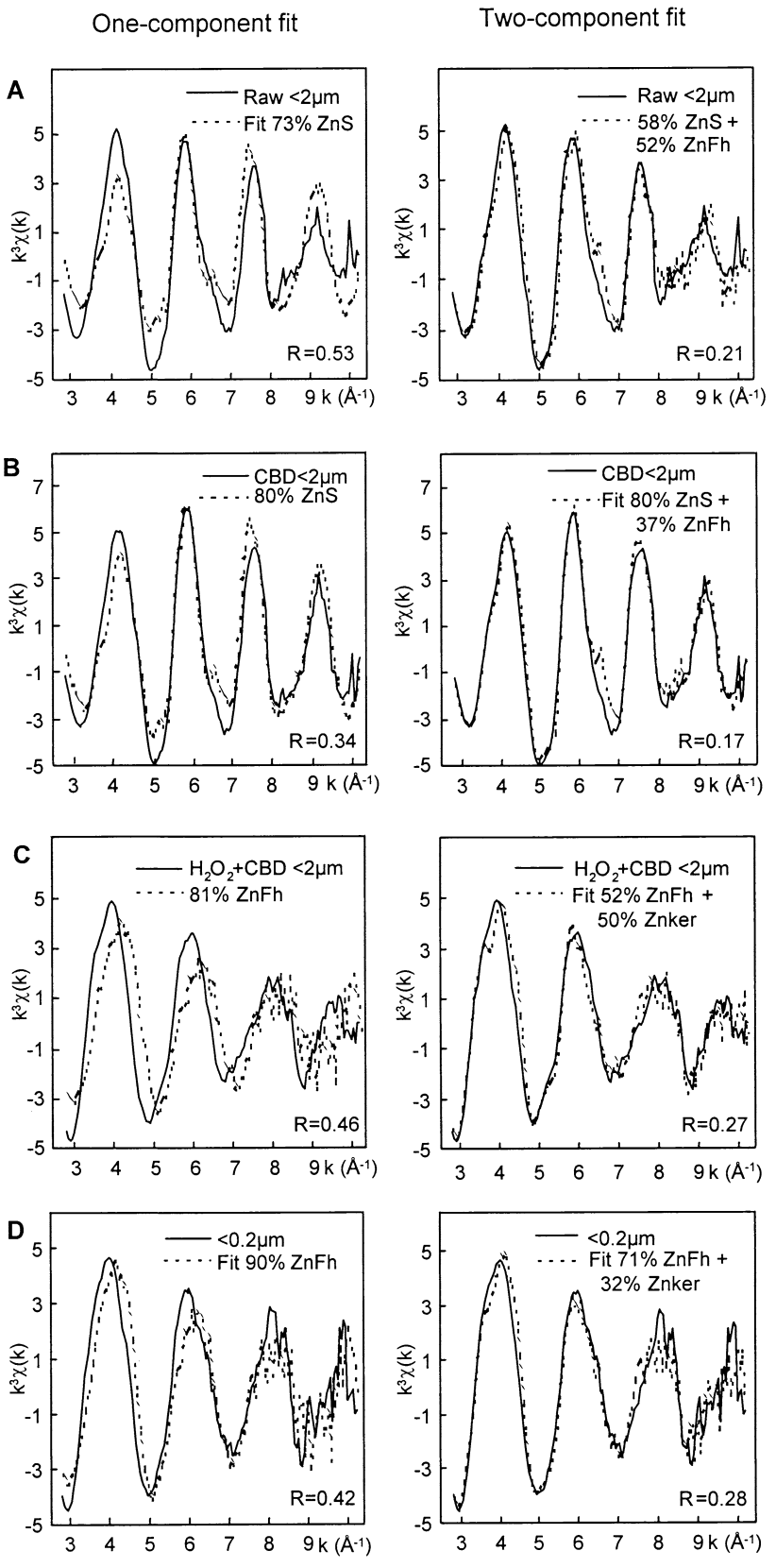

Fig. 15. Least squares fit of extended X-ray absorption fine structure spectroscopy spectra for samples from the clay and fine fraction with one, or a combination of two, Zn references (ZnS, ZnFh, and ZnKer).

Table 4. Nature and proportion[a] of Zn species and techniques applied for each sediment sample.

Sample	ZnS (%)	ZnFh (%)	Willemite (%)	ZnKer (%)	ZnO (%)	R^b	XRD	EXAFS	P-EXAFS	μ-PIXE	μ-SXRF
Raw sediment	73	40				0.18	X	X			
Powder from coarse fraction											
DGC (Dry-ground coarse fraction)	52	30	20			0.20	X	X			
WGC (Wet-ground coarse fraction)	22	42	40			0.25	X	X			
NPBS (Nonporous black slags)	103					0.27	X	X			
PBS (Porous black slags)	83	36				0.19	X	X			
CG (Colored grains)	51	36	19			0.22	X	X			
NPBS + PBS + CG[c]	69	20	3								
Individual grains from coarse fraction											
NPBSg1 (Nonporous black slag grain 1)	115					0.24		X		X	
NPBSg2 (Nonporous black slag grain 2)	115					0.24		X		X	
PBSg (Porous black slag grain)	77	30				0.19		X		X	
CGg (Colored grain grain)					62	0.23		X		X	
Fine fractions											
Raw < 2 μm	58	52				0.21	X		X		X
CBD < 2 μm (CBD-treated < 2 μm)	80	37				0.17	X		X		X
H_2O_2 + CBD < 2 μm (H_2O_2 and CBD-treated < 2 μm)		52		50		0.27	X		X		
<0.2 μm		71		32		0.28			X		

XRD = X-ray diffraction, EXAFS = extended X-ray absorption fine structure, P-EXAFS = polarized EXAFS, μ-PIXE = micro-particle-induced X-ray emission, μ-SXRF = micro-synchrotron-based X-ray radiation fluorescence, CBD = sodium bicarbonate–buffered ditrionite-citrate solution.

[a] Fit percentages were not normalized to 100%.

[b] R is the best-fit criterion: $R = \Sigma|(k^3\chi\text{exp} - k^3\chi\text{model})|/\Sigma|k^3\chi\text{exp}|$. The precision on the proportion of Zn species is ~10%.

[c] Sum of the three types of grain weighted by the proportion of Zn.

transported in air from the chimneys of the nearby foundries because 70% of particles emitted from chimney stacks are usually <10 μm in size (Sobanska et al., 1999). Coarse grains likely result from the erosion of the nearby slag tailings (Loyaux-Lawniczak, 1999; Sobanska, 1999) or from ore and slag shipping in canals. When dredged sediments are deposited on soils, the oxidation of ZnS releases soluble Zn, and this process constitutes a potential hazard for aquifers and plants (Sarret et al., 1998; Salt et al., 1999; Marseille et al., 2000). The sorption of dissolved Zn by soil constituents, such as Fe (oxyhydr)oxides and phyllosilicates, or its precipitation with other solutes can decrease this hazard. In terrestrial waters, the silica concentration is largely controlled by the solubility of quartz (11 ppm; Rimstidt, 1997) and amorphous silica (116 ppm; Rimstidt and Barnes, 1980). In this context, solutions percolating in Zn-contaminated soils are supersaturated or near saturation with respect to Zn-phyllosilicate, and this constituent can readily precipitate, for instance, on quartz surfaces (Manceau et al., 1999, 2000), thereby reducing the mobility of Zn. Dissolved Zn and Si concentrations and the pH value measured after equilibrating our sediment for 24 h in deionized water, filtration to 0.45 μm, and acidification in concentrated HCl, were 1.2 $\pm$ 0.12 mg/L, 5.2 $\pm$ 0.22 mg/L, and 7.2, respectively. Placing these values in the $[Zn]_{aq} = f(\text{pH})$ equilibrium diagram for Zn phyllosilicate (Fig. 26 in Manceau et al., 2000) suggested that dissolved Zn was actually saturated with respect to phyllosilicates. In addition to the overwhelming presence of quartz and amorphous silica in soils, which can provide enough dissolved silica to immobilize Zn, contaminated sediments often contain pyrite. Under oxidizing conditions, pyrite releases ferric iron, which precipitates as hydrous (oxyhydr)oxides having a high surface reactivity and affinity for metals. This study suggests that these two physicochemical processes (i.e., Zn-Si precipitation and Zn sorption on ferrihydrite) operate in the present sediment and contribute to reduce Zn mobility.

5. CONCLUSION

In this study, we succeeded in qualitatively and quantitatively speciating Zn-bearing mineral phases in a smelter-affected sediment. Three Zn minerals released in the environment by smelting plants were identified, sphalerite, willemite, and zincite, in decreasing order of abundance. Zinc released by the weathering of these primary minerals is bound predominantly to Fe (oxyhydr)oxides and, to a lesser extent, to phyllosilicates. Identifying trace metal species in natural matrices is complex and requires the combined use of structural and chemical techniques. In this work, EXAFS spectroscopy, complemented by a rigorous mathematical analysis of EXAFS spectra using a PCA and LSF procedure, was employed in combination with size fractionation, chemical treatments, and laterally resolved techniques, namely, μ-PIXE and μ-SXRF. This meaningful and multitechnique study provides a baseline for further quantitative studies on the speciation of metals in dilute and multicomponent systems of environmental relevance.

Acknowledgments—The authors are grateful to John Bargar and two anonymous reviewers for their constructive comments and to Dr. Garrison Sposito for his editorial handling. We acknowledge O. Proux on BM32 at the European Synchrotron Radiation Facility (ESRF) in Grenoble, France, and A. McDowell and R. Celestre on 10.3.2 at the Advanced Light Source (ALS) in Berkeley, California, for their assistance in the collection of X-ray absorption spectra. We also acknowledge L. Daudin and the staff of the Laboratoire Pierre Süe (LPS) for their assistance in collecting and treating PIXE data. We are grateful to the ESRF, the ALS, and the LPS for the provision of beam time.

Associate editor: G. Sposito

REFERENCES

Bertsch P. M., Hunter D. B., Nuessle P. R., and Clark S. B. (1997) Molecular characterization of contaminants in soils by spatially resolved XRF & XANES spectroscopy. *J. Phys. IV* **C2,** 817–818.

Bigham J. M., Schwertmann U., Traina S. J., Winland R. L., and Wolf M. (1996) Schwertmannite and the chemical modeling of iron in acid sulfate waters. *Geochim. Cosmochim. Acta* **60,** 2111–2121.

Castaner R. and Prieto C. (1997) Fluorescence detection of extended X-ray absorption fine structure in thin films. *J. Phys. III* **7,** 337–349.

Cornell R. M. and Schwertmann U. (1996) *The Iron Oxides: Structure, Properties, Reactions, Occurrence and Uses*. VCH Publishers, New York.

Davis J. A. and Kent D. B. (1990) Surface complexation modeling in aqueous geochemistry. In *Reviews in Mineralogy, Vol. 23: Mineral-Water Interface Geochemistry* (eds. M. F. Hochella, Jr., and A. F. White), pp. 177–260. Mineralogical Society of America, Washington, DC.

Davison W. (1991) The solubility of iron sulfides in synthetic and natural waters at ambient temperatures. *Aquat. Sci.* **53/54,** 309–329.

Dyrssen D. and Kremling K. (1990) Increasing hydrogen sulfide concentration and trace metal behavior in the anoxic baltic waters. *Mar. Chem.* **24,** 143–153.

Fay M. J., Proctor A., Hoffmann D. P., Houalla M., and Hercules D. M. (1992) Determination of the Mo surface environment of Mo/TiO_2 catalysts by EXAFS, XANES and PCA. *Mikrochim. Acta* **109,** 281–293.

Hammade N. V. (2000) *Caractérisation et valorisation des déchets et sous-produits industriels dans le domaine du génie civil et en technique routière*. Ph.D. thesis, Université des Sciences et Technologies de Lille, France.

Hazemann J. L., Nayouf K., and De Bergevin F. (1995) Modelisation by finite elements of sagittal focusing. *Nucl. Instrum. Methods* **B97,** 547–550.

Hesterberg D., Sayers D. E., Zhou W., Plummer G. M., and Robarge W. P. (1997) X-ray absorption spectroscopy of lead and zinc speciation in a contaminated groundwater aquifer. *Environ. Sci. Technol.* **31,** 2840–2846.

Hochella M. F., Moore J. N., Golla U., and Putnis A. (1999) A TEM study of samples from acid mine drainage systems: metal-mineral association with implications for transport. *Geochim. Cosmochim. Acta* **63,** 3395–3406.

Isaure M. P., Laboudigue A., Manceau A., Sarret G., Tiffreau C., and Trocellier P. (2001) Characterisation of zinc in slags issued from a contaminated sediment by coupling μPIXE, μRBS, μEXAFS and powder EXAFS spectroscopy. *Nucl. Inst. Meth. Phys. Res.* **181,** 598–602.

Jackson M. L. (1985) *Soil Chemical Analysis—Advanced Course*, 2nd ed. M. L. Jackson, Madison, WI.

Loyaux-Lawniczak S. (1999) *Mécanismes d'immobilisation du chrome dans les sols: Diagnostic de la pollution d'une friche industrielle et réactivité des ions chromates vis-à-vis du fer divalent*. Ph.D. thesis, Université Henri Poincaré, Nancy I, France.

Malinowski E. R. (1991) *Factor Analysis in Chemistry*. John Wiley, New York.

Manceau A. and Combes J. M. (1988) Structure of Mn and Fe oxides and oxyhydroxides: A topological approach by EXAFS. *Phys. Chem. Miner.* **15,** 283–295.

Manceau A. and Schlegel M. L. (2001) Texture effect on polarized EXAFS amplitude. *Phys. Chem. Miner.* **28,** 52–56.

Manceau A., Bonnin D., Stone W. E. E., and Sanz J. (1990) Distribution of Fe in the octahedral sheet of trioctahedral micas by polarized EXAFS. Comparison with NMR results. *Phys. Chem. Miner.* **17,** 363–370.

Manceau A., Boisset M. C., Sarret G., Hazemann J. L., Mench M., Cambier P., and Prost R. (1996) Direct determination of lead speciation in contaminated soils by EXAFS spectroscopy. *Environ. Sci. Technol.* **30,** 1540–1552.

Manceau A., Chateigner D., and Gates W. P. (1998) Polarized EXAFS, distance-valence least-squares modeling (DVLS), and quantitative texture analysis approaches to the structural refinement of Garfield nontronite. *Phys. Chem. Miner.* **28,** 347–365.

Manceau A., Schlegel M. L., Nagy K. L., and Charlet L. (1999) Evidence for the formation of trioctahedral clay upon sorption of Co^{2+} on quartz. *J. Colloid Interface Sci.* **220,** 181–197.

Manceau A., Lanson B., Schlegel M. L., Hargé J. C., Musso M., Eybert-Bérard L., Hazemann J. L., Chateigner D., and Lamble G. M. (2000) Quantitative Zn speciation in smelter-contaminated soils by EXAFS spectroscopy. *Am. J. Sci.* **300,** 289–343.

Marseille F., Tiffreau C., Laboudigue A., and Lecomte P. (2000) Impact of vegetation on the mobility and bioavailability of trace elements in a dredged sediment deposit: A greenhouse study. *Agronomie* **20,** 547–556.

Martinez C. E. and McBride M. B. (1998) Solubility of Cd^{2+}, Cu^{2+}, Pb^{2+} and Zn^{2+} in aged coprecipitates with amorphous iron hydroxides. *Environ. Sci. Technol.* **32,** 743–748.

Maxwell J. A., Campbell J. L., and Teesdale W. J. (1989) The Guelph PIXE software package. *Nucl. Instrum. Meth. B* **43,** 218–230.

McDowell A. A., Lamble C. M., Celestre R. S., Patel J. R., and Padmore H. A. (1998) Progress towards sub-micron hard x-ray imaging using elliptically bent mirrors and its implications. In *SPIE Conference on X-ray Microfocusing: Applications and Techniques*, 3449, pp. 137–144. San Diego, CA, July 1998.

Mehra O. P. and Jackson M. L. (1960) Iron oxide removal from soils and clays by a dithionite-citrate system buffered with sodium bicarbonate. In *Proceedings of the Seventh National Conference on Clays and Clay Minerals*, pp. 317–327. Pergamon Press, London.

Mesjasz-Przybylowicz J., Grodzinska K., Przybylowicz W. J., Godzik B., and Lukaszewska G. S. (1999) Micro-PIXE studies of elemental distribution in seeds of silene vulgaris from a zinc dump in Olkusz, southern Poland. *Nucl. Instrum. Meth. B* **58,** 306–311.

O'Day P. A., Carroll S. A., and Waychunas G. A. (1998) Rock-water interactions controlling zinc, cadmium, and lead concentrations in surface waters and sediments, US Tri-State Mining District. 1: Molecular identification using X-ray absorption spectroscopy. *Environ. Sci. Technol.* **32,** 943–955.

O'Day P. A., Carroll S. A., Randall S., Martinelli R. E., Anderson S. L., Jelinski J., and Knezovich J. P. (2000) Metal speciation and bioavailability in contaminated estuary sediments, Alameda Naval Air Station, California. *Environ. Sci. Technol.* **34,** 3665–3673.

Ostergren J. D., Brown G. E., Jr., Parks G. A., and Tingle T. N. (1999) Quantitative speciation of lead in selected mine tailings from Leadville, CO. *Environ. Sci. Technol.* **33,** 1627–1636.

Parkman R. H., Curtis C. D., Vaughan D. J., and Charnock J. M. (1996) Metal fixation and mobilisation in the sediments of Afon Goch estuary—Dulas Bay, Anglesey. *Appl. Geochem.* **11,** 203–210.

Quevauviller P., Rauret G., Muntau H., Ure A. M., Rubio R., Lopez-Sanchez J. F., Fiedler H. D., and Griepink B. (1994) Evaluation of a sequential extraction procedure for the determination of extractable trace metal contents in sediments. *Fresenius J. Anal. Chem.* **349,** 808–814.

Ressler T., Wong J., Roos J., and Smith I. L. (2000) Quantitative speciation of Mn-bearing particulates emitted from autos burning (methylcyclopentadienyl) manganese tricarbonyl-added gasolines using XANES spectroscopy. *Environ. Sci. Technol.* **34,** 950–958.

Rimstidt J. D. (1997) Quartz solubility at low temperatures. *Geochim. Cosmochim. Acta* **61,** 2553–2558.

Rimstidt J. D. and Barnes H. L. (1980) The kinetics of silica-water reactions. *Geochim. Cosmochim. Acta* **44,** 1683–1699.

Salt D. E., Prince R. C., Baker A. J. M., Raskin I., and Pickering I. J. (1999) Zinc ligands in the metal hyperaccumulator *Thlaspi caerulescens* as determined using X-ray absorption spectroscopy. *Environ. Sci. Technol.* **33,** 713–717.

Sarret G., Manceau A., Cuny D., VanHaluwyn C., Déruelle S., Hazemann J. L., Soldo Y., Eybert-Bérard L., and Menthonnex J. J. (1998) Mechanisms of lichen resistance to metallic pollution. *Environ. Sci. Technol.* **32,** 3325–3330.

Schlegel M. L., Manceau A., Chateigner D., and Charlet L. (1999) Sorption of metal ions on clay minerals. I. Polarized EXAFS evidence for the adsorption of Co on the edges of hectorite particles. *J. Colloid Interface Sci.* **215,** 140–158.

Schlegel M. L., Manceau A., Charlet L., Chateigner D., and Hazemann J. L. (2001a) Sorption of metal ions on clay minerals. III. Nucleation and growth of Zn phyllosilicate on the edges of hectorite. *Geochim. Cosmochim. Acta* **65,** 2854–2859.

Schlegel, M. L., Manceau A., Charlet, L., and Hazemann, J. L. (2001b)

Adsorption mechanism of Zn on hectorite as a function of time, pH, and ionic strength. *Am. J. Sci.* (in press).

Shuman L. M. (1978) Zinc, manganese, and copper in soil fractions. *Soil Sci.* **127,** 10–17.

Singh S. P., Tack F. M., and Verloo M. G. (1998) Heavy metal fractionation and extractability in dredged sediment derived surface soils. *Water Air Soil Pollut.* **102,** 313–328.

Sobanska S. (1999) *Etude de la spéciation du plomb et du zinc dans des poussières industrielles et dans un sol contaminé*. Ph.D. thesis, Université des Sciences et Technologies de Lille, France.

Sobanska S., Ricq N., Laboudigue A., Guillermo R., Brémard C., Laureyns J., Merlin J. C., and Wignacourt J. P. (1999) Microchemical investigations of dust emitted by a lead smelter. *Environ. Sci. Technol.* **33,** 1334–1339.

Song Y., Wilson M. J., Moon H. S., Bacon J. R., and Bain D. C. (1999) Chemical and mineralogical forms of lead, zinc and cadmium in particle size fractions of some wastes, sediments and soils in Korea. *Appl. Geochem.* **14,** 621–633.

Spadini L., Manceau A., Schindler P. W., and Charlet L. (1994) Structure and stability of Cd^{2+} surface complexes on ferric oxides. *J. Colloid Interface Sci.* **168,** 73–86.

Stumm W. and Morgan J. J. (1996) *Aquatic Chemistry: Chemical Equilibria and Rates in Natural Waters*. Wiley Interscience, New York.

Teo B. K. (1986) *EXAFS: Basic Principles and Data Analysis*. Springer, Berlin, Germany.

Tessier A., Campbell P. G. C., and Bisson M. (1979) Sequential extraction procedure for the speciation of particulate trace metals. *Anal. Chem.* **51,** 844–851.

Thiry M. and Van Oort F. (1999) Les phases minérales majeures et mineures d'une friche industrielle de métallurgie des métaux non-ferreux: État d'altération, évolution géochimique et devenir des métaux polluants du site de Mortagne-du-Nord. In *Spéciation des métaux dans le sol*, pp. 108–135. Publications Ecrin, Paris, France.

Tiffreau C., Marseille F., Isaure M. P., Lors C., Laboudigue A., Branchu P., and Lecomte P. (1999) Impact of contaminated dredged sediment deposits on clean soils: An interdisciplinary study of the mobility and bioavailability of the metallic pollution. In *4th Conference on Characterisation and Treatment of Sediments (CATS)*, Antwerp, Belgium, September 15-17, Eds De Schutter G, 243–252.

Trocellier P. (1996) Theoretical and practical aspects of nuclear microprobe analysis of solid surfaces and bulk solids. *Microsc. Microanal. Microstruct.* **7,** 235–254.

Troger L., Arvanitis D., Baberschke K., Michaelis H., Grimm U., and Zschech E. (1992) Full correction of the self-absorption in soft-fluorescence extended x-ray-absorption fine structure. *Phys. Rev. B* **46,** 3283–3289.

Wasserman S. R. (1997) The analysis of mixtures: Application of principal component analysis to XAS spectra. *J. Phys. IV* **7,** 203–205.

Wasserman S. R., Allen P. G., Shuh D. K., Bucher J. J., and Edelstein N. M. (1999) EXAFS and principal component analysis: A new shell game. *J. Synchrotron Rad.* **6,** 284–286.

Webb S. M., Leppard G. G., and Gaillard J. F. (2000) Zinc speciation in a contaminated aquatic environment: Characterization of environmental particles by analytical electron microscopy. *Environ. Sci. Technol.* **34,** 1926–1933.

Xenophontos L., Stevens G., and Przybylowicz W. J. (1999) Micro-PIXE elemental imaging of pyrites from the Bulawayan-Bubi Greenstone Belt, Zimbabwe. *Nucl. Instrum. Meth. B* **150,** 496–501.